

# Attention Mechanism for Lithium-Ion Battery Lifespan Prediction: Temporal and Cyclic Attention

Jaewook Lee<sup>1</sup>, Seongmin Heo<sup>1</sup>, Jay H. Lee<sup>1, 2, 3, \*</sup>

<sup>1</sup>Department of Chemical and Biomolecular Engineering, Korea Advanced Institute of Science and Technology, 291 Daehak-ro, Yuseong-gu, Daejeon 34141, Republic of Korea

<sup>2</sup>Mork Family Department of Chemical Engineering and Materials Science, University of Southern California, 3651 Watt Way, Los Angeles, CA 90089, United States

<sup>3</sup>Lead Contact

\*Correspondence. E-mail address: [jlee4140@usc.edu](mailto:jlee4140@usc.edu) (J.H. Lee).

## Highlights

- Utilized attention mechanisms considering cyclic properties of degradation dataset
- Utilized multi-head attention to understand LIB degradation in various aspects
- Analyzed different crucial timesteps and cycles from each batch
- Reduced input size to 30 cycles for knee-onset prediction

## Context & Scale

With the recent success of lithium-ion batteries, lots of researches are conducted focusing on fast charging of lithium-ion batteries. However, it can cause catastrophic side reactions such as Li plating which would lead the battery degrade rapidly from a certain point. This study aims to predict the knee, the point at which rapid and nonlinear degradation begins. In the process, we build a model that takes both intra- and inter-cycle behavior into account, taking advantage of the fact that batteries are cyclic datasets that are repeatedly charged and discharged. Using a technique called Attention mechanism, we extract the time points and cycles that have a significant impact on the degradation and determine whether they are actually significant, rather than simply predicting the knee value. Based on the key cycle information, we also reduce the input size required for prediction, making it possible to predict the lifetime with less cost in real-world battery applications.

## Summary

Accurately predicting lithium-ion batteries (LIBs) lifespan is pivotal for optimizing usage and preventing accidents. Previous approaches often relied on inputs challenging to measure in real-time, and failed to capture intra- and inter-cycle data patterns simultaneously. Our study employ attention mechanisms (AM) to develop data-driven models predicting LIB lifespan using easily measurable inputs. Developed model integrates recurrent neural network and convolutional neural network, featuring two types of AMs: temporal attention (TA) and cyclic attention (CA). TA identifies important time steps within each cycle, CA strives to capture key features of inter-cycle correlations through self-attention (SA). We apply the developed model to publicly available data consisting of three batches of cycling modes. TA scores highlight the “rest” phase as a key characteristic to distinguish different batches. By leveraging CA scores, we decreased the input dimension from 100 cycles to 50 and 30 cycles with single- and multi-head attention.

## Keywords

Lithium-ion Batteries, Lifespan Prediction, Cyclic Behaviors, Attention Mechanism, Explainable Artificial Intelligence, Convolutional Neural Networks, Recurrent Neural Networks, Input Reduction

## Introduction

As the electric vehicle (EV) market continues to evolve, the importance of the battery management system (BMS) is increasingly prominent. The BMS plays a pivotal role in overseeing the operations of lithium-ion batteries (LIBs) based on real-time measurements<sup>1</sup>. An integral aspect of this system is the accurate prediction of battery lifespan, leveraging the gathered measurements. This predictive capability serves as a valuable tool for users, enabling them to tailor the battery operation to enhance longevity and safety<sup>2</sup>. Furthermore, it offers guidance for achieving optimal battery performance in challenging environmental conditions, such as extremely low and extremely high temperatures.

Conventionally, a LIB is considered to reach its end-of-life (EOL) when the state of health (SOH), defined as the ratio of the current capacity to its nominal capacity, falls to 80%<sup>3</sup>. As the LIB approaches its EOL, the risk of safety accidents, including fire and explosion, escalates<sup>4</sup>, underscoring the critical nature of accurate lifespan predictions. However, predicting LIB lifespan proves challenging due to the intricate interplay among various LIB degradation mechanisms, such as Li plating, dendrite formation, electrolyte decomposition, and solid electrolyte interphase formation<sup>5</sup>.

Current LIB lifespan prediction models fall into two main categories: physics-based and data-driven. Physics-based models are constructed based on a thorough understanding of LIB degradation mechanisms. Noteworthy models of this category include the equivalent circuit model<sup>6</sup> and electrochemical model<sup>7</sup>. These models offer the advantages of high interpretability and extrapolation, albeit limited to the specific phenomena considered during their development. Presently, constructing a comprehensive and precise physics-based model for LIB lifespan, encompassing all crucial LIB degradation mechanisms<sup>8</sup>, remains an exceptionally challenging task.

The rise of data-driven models in lifespan prediction is evident, as they forecast the lifespan solely based on data, eliminating the need for detailed knowledge about LIB degradation mechanisms<sup>9</sup>. Simple examples of such models include elastic net (EN), Gaussian process regression, and support vector regression<sup>10-12</sup>. Recently, neural networks, including various combinations of types such as convolutional neural network (CNN) and recurrent neural network (RNN), have gained popularity as lifespan prediction models<sup>13,14</sup>. Additionally, researchers have explored ensembles of different machine learning methods<sup>15,16</sup>. Despite extensive research, several challenges persist in this approach. Notably, the literature has not thoroughly investigated features related to cycle-to-cycle behavior in cycling data, which could be crucial for understanding the underlying characteristics of LIB operation data. In response, the authors have proposed a data processing strategy capable of simultaneously extracting intra-cycle and inter-cycle features using combinations of RNNs and CNNs<sup>17</sup>.

Enhancing their interpretability is another ongoing challenge in advancing data-driven LIB lifespan prediction models. In deep learning literature, attention mechanisms (AM), initially proposed in natural language processing (NLP), are frequently employed to discern essential and/or irrelevant aspects of the data<sup>18,19</sup>. AM has demonstrated success in various tasks, including image captioning<sup>20</sup>, image-text matching<sup>21</sup>, and time series modeling<sup>22,23</sup>, often in conjunction with RNNs<sup>24</sup>. AM has also found application in LIB lifespan prediction. For instance, in Yang et al.<sup>25</sup>, dual-stage attention was used to estimate the state of charge (SOC). The first stage of AM extracts a robust refined health index (RHI) from the direct health index (DHI). Subsequently, RNN-based models, such as long short-term memory (LSTM)<sup>26</sup> and gated recurrent unit (GRU)<sup>27</sup>, are constructed, and temporal attention (TA) is applied to correlate crucial time steps. Zhao et al.<sup>28</sup> applied AM to estimate the SOH of LIBs. After extracting 11 health indexes from LIB operation data, GRUs are built, and AM is employed to extract key hidden states for accurate SOH estimation. In Jiang et al.<sup>29</sup>, self-attention (SA) is used to extract critical features. In Wei et al.<sup>30</sup>, a graph of input features is optimized for SOH and remaining useful life (RUL) estimation, incorporating a dual attention mechanism. While AM has proven valuable in enhancing

model performance, there remains a lack of extensive analysis of attention scores, which is crucial for understanding the utility of AM. Additionally, the cyclic properties of the data have not been thoroughly and coherently considered in these works.

Proper analysis of AM results holds the potential to decrease the size of input data significantly, i.e., the number of operation cycles incorporated into the model input necessary for constructing accurate prediction models. This, in turn, facilitates early-stage lifespan prediction. Notable attempts, such as the one documented in Xiong et al.<sup>31</sup>, aimed to reduce the input size in comparison to Severson et al.<sup>10</sup>. In our another prior research<sup>32</sup>, we used EN to reduce the input size. Specifically, when employing 2D CNN, we successfully reduced the data size to 85 cycles (from 100 cycles used in Severson et al.<sup>10</sup>) without compromising model accuracy. However, a systematic procedure for reducing the input size is currently lacking; in previous works, the sizes were often chosen arbitrarily or determined through trial and error.

In this study, we leverage the dataset from Severson et al.<sup>10</sup> to construct an interpretable lifespan prediction model. Our methodology integrates TA and cyclic attention (CA) into the RNN + 1D CNN model proposed in our previous work<sup>17</sup>. Initially, TA is incorporated into the model to discern crucial time steps within each cycle from the hidden state sequence. Subsequently, we explore two attention techniques for CA: SA and multi-head attention (MHA). SA is employed to extract cycle-to-cycle features crucial for lifespan prediction, while MHA is introduced to analyze the intricate nonlinear relationships between inputs and outputs, thereby enhancing the prediction performance of the model. We also demonstrate how attention scores can systematically reduce the input data size. All acronyms and nomenclatures used in this paper are summarized before References.

## Results and Discussion

We suggest several knee-onset regression models for LIBs that encapsulate the crucial characteristics of intra- and inter-cycle behaviors inherent in LIB degradation data. These models leverage *temporal attention* (TA), *self-attention* (SA), and *multi-head attention* (MHA). TA is used to gauge correlations between different time steps within the same cycle to capture relevant features of intra-cycle trends, which entail dynamic variations within each cycle. TA mitigates the VG problem by using the entire hidden state sequence to calculate the context vector, serving as input to the 1D CNN. Notably, the RNN – 1D CNN model without TA encounters the VG problem, relying solely on the last hidden state of each cycle as the context vector. To capture relevant features from inter-cycle trends, i.e., cycle-to-cycle changes in the profiles, we introduce *cyclic attention* (CA), a combination of SA and MHA. As previously discussed, SA is applied to the context vectors of all the cycles to assess similarities between cycles. Leveraging the key-query relationships identified by SA, crucial cycles for knee-onset regression can be discerned. Subsequently, MHA is applied to measure similarities between context vectors from various viewpoints.

[Figure 1](#) illustrates the proposed model structures incorporating attention mechanisms. In all models, the RNN calculates the encoded values of the hidden state sequence, denoted as  $\mathbf{h}_1, \dots, \mathbf{h}_{n_{cy}}$ , for each cycle. The model depicted in [Figure 1A](#), referred to as the RNN + TA + 1D CNN model, uses these encoded values to calculate TA scores of all hidden states in the sequence. The representative context vector for each cycle is then derived as a linear sum, weighted by the TA scores, effectively reducing memory requirements. Inspection of the TA scores reveals crucial time steps with significant implications for knee-onset prediction.

The second model, denoted as the RNN + CA + 1D CNN model and illustrated in [Figure 1B](#), integrates the baseline RNN + 1D CNN model with CA. In this configuration, the context vector comprises the last hidden state of the RNN for each cycle, and SA is applied to assess the similarities between these context vectors. It assigns elevated weights to significant cycles, generating refined context vectors  $\tilde{\mathbf{ct}}_1, \dots, \tilde{\mathbf{ct}}_{n_{cy}}$  from raw context vectors  $\mathbf{ct}_1, \dots, \mathbf{ct}_{n_{cy}}$  (output from the RNN). The adjustment enables the cycle-to-cycle relationship to be reflected before feeding the context vectors into the CNN. The context vectors are derived from either the last hidden state or the context vector after applying TA to the entire hidden state sequence. An optimal input dimension can be determined by analyzing the CA score from this model.

By combining the merits of both TA and CA, we introduce the RNN + TA + CA + 1D CNN model, illustrated in [Figure 1C](#). In this model, the context vector is derived using TA scores, akin to the first model, rather than relying solely on the last hidden state of the RNN. This context vector is then employed by the CA. By comparing the outcomes of the three models, we can systematically explore the advantages of TA and CA and their collaborative effectiveness in our problem. Furthermore, MHA is incorporated into the RNN + TA + CA + 1D CNN model to evaluate its efficacy. Details of TA, SA, and MHA are suggested in Experimental Procedures.

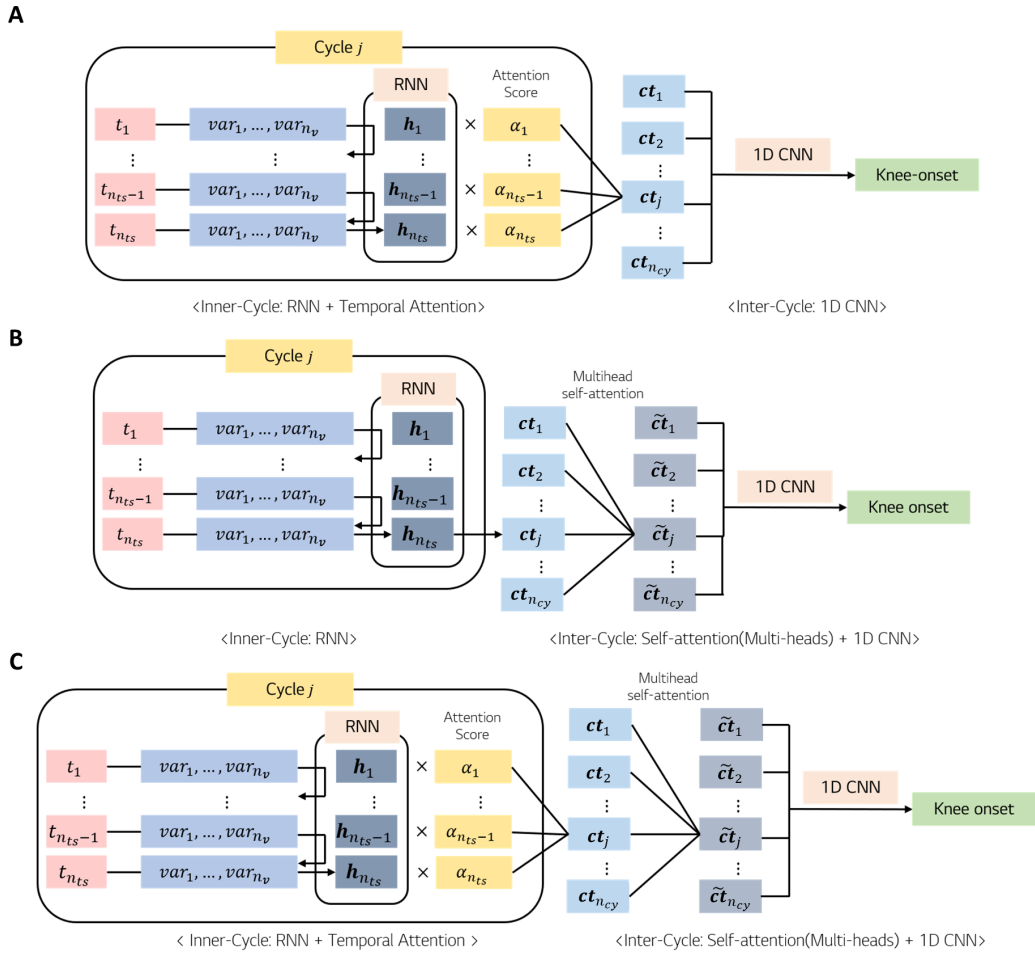


**Figure 1. Attention-based model structures proposed in this study. (A) RNN + TA + 1D CNN, (B) RNN + CA + 1D CNN, (C) RNN + TA + CA + 1D CNN.**

In this section, we will present the analysis results for two problems utilizing the dataset from Severson et al.<sup>10</sup>, commonly known as the *Severson dataset*. The initial focus is knee-onset prediction leveraging data from the first 100 charging-discharging cycles. This will be followed by examining the feasibility of reducing the input dimension based on cyclic attention scores, potentially utilizing data from a more limited number of initial cycles.

We employed three distinct datasets (charging only, discharging only, and the combined dataset including rest periods) extracted from the Severson dataset as in our previous work<sup>17</sup>. To assess the performance of the different models, we partitioned the data into training, validation, and test sets. Root mean square errors (RMSE) of the test set serve as regression performance metrics, which will be examined based on the TA and CA scores in the subsequent section. Additional information about the Severson dataset is provided in [Note S1](#), while the specifics of how the dataset is partitioned into training, validation, and test sets are given in the Experimental Procedures.

### 100-cycle scenario

To assess the impact of the rest phase on the TA scores, we experimented with two additional datasets (charging only and discharging only) alongside the entire dataset, which includes the rest periods. [Table 1](#) illustrates the performance of the baseline models (i.e., the RNN + 1D CNN and RNN + 2D CNN) and the RNN + TA + 1D CNN model. Across all dataset configurations, the RNN + TA + 1D CNN and RNN + 2D CNN models exhibited lower test losses than the baseline model, primarily by

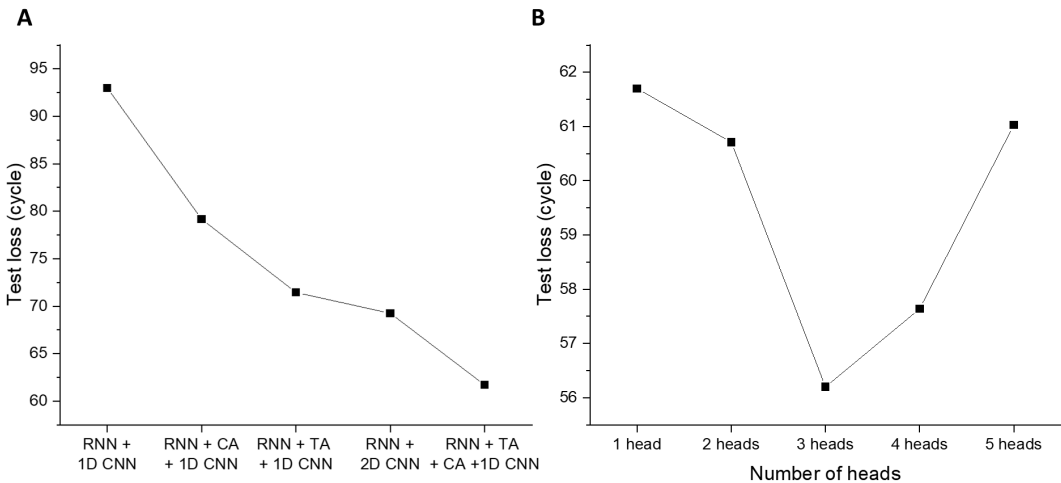
mitigating the VG effect observed in the latter. Among the dataset options, the combined dataset containing data from all charge, rest, and discharge phases is used as inputs for the subsequent experiments.

**Table 1.** Regression performance of RNN + 1D CNN, RNN + 2D CNN and RNN + TA + 1D CNN (Charging only, Discharging only, Combined dataset)

Test loss (RMSE)	Charging only	Discharging only	Combined dataset
RNN + 1D CNN	149.46	98.39	93.10
RNN + 2D CNN	91.94	70.68	69.25
RNN + TA + 1D CNN	<b>84.75</b>	<b>71.65</b>	<b>71.44</b>

In [Figure 2A](#), the performance of the RNN + CA + 1D CNN model is observed to be superior to the RNN + 1D CNN model. This improvement is attributed to considering similarities between cycles in the context vectors constructed by the SA before applying 1D CNN to them. However, owing to the presence of VG, the performance is inferior to models not affected by VG-induced degradation, such as the RNN + 2D CNN or RNN + TA + 1D CNN. While creating a context vector considering the cyclic property is crucial, the limited regression performance is apparent when applying CA solely to the last hidden states, which have lost significant information about transient profiles due to VG.

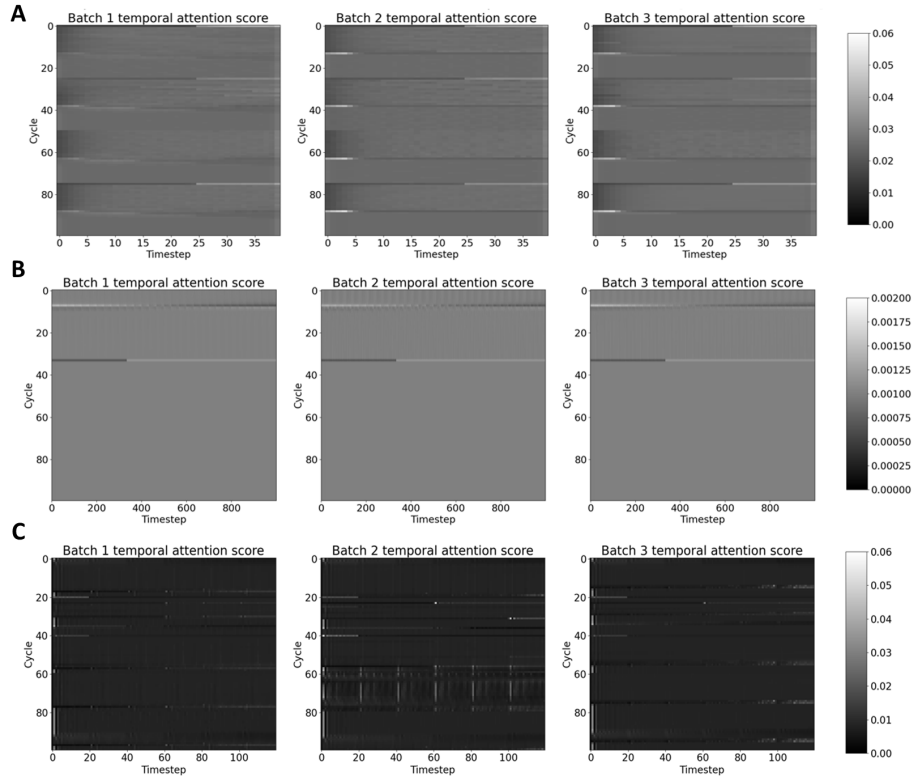
Next, we compare the performance of RNN + TA + CA + 1D CNN (SHA) with RNN + CA + 1D CNN (SHA) and RNN + TA + 1D CNN. [Figure 2A](#) also illustrates that RNN + TA + CA + 1D CNN outperformed the other four models, showcasing effective synergy between TA and SA. [Figure 2B](#) presents the regression results with different numbers of heads. Regardless of the number of heads, MHA exhibited superior performance to SHA, with three heads proving to be the most effective.



**Figure 2.** (A) Regression performance of baseline and proposed models (SHA for CA), (B) Regression performance of RNN + TA + CA + 1D CNN with MHA.

[Figure 3](#) displays the TA scores of cells in each batch across the three datasets (charging only, discharging only, and combined dataset). [Figure 3A-B](#) present TA scores for the charging-only and discharging-only datasets, showing minimal difference among the batches. Consequently, when utilizing these datasets, it can be inferred that incorporating TA into the RNN + 1D CNN improves performance solely by alleviating the VG problem. In contrast, [Figure 3C](#) (combined dataset) reveals distinct trends in TA scores for Batch 2 compared to Batches 1 and 3. For Batch 2, high TA scores are observed around time step 20 for cycles 60-80, corresponding to the rest after charging to 80% SOC.

Similar observations are made around time step 100, corresponding to the rest period after discharging concludes. These observations underscore the pivotal role of “rest time” in LIB lifespan prediction, justifying the consideration of only the combined dataset is considered for further experiments.



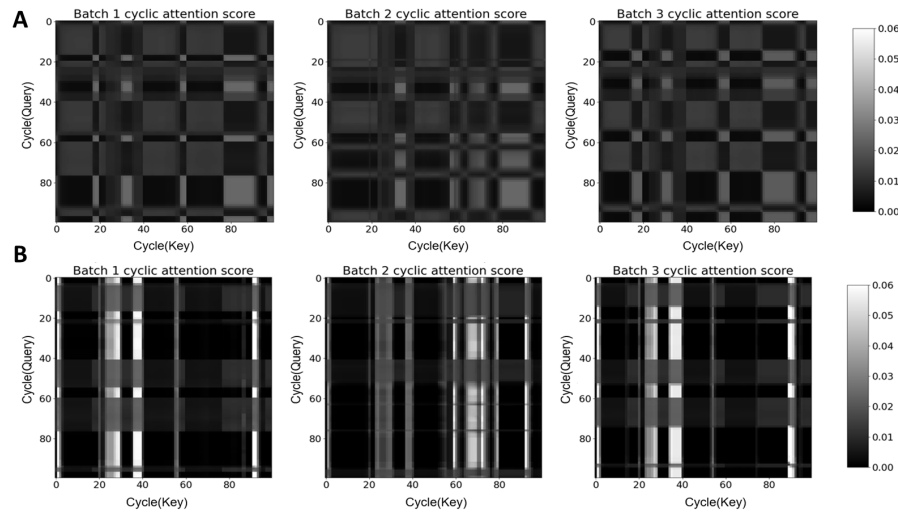
**Figure 3. TA scores of RNN + TA + 1D CNN with different datasets.** (A) Charging only dataset, (B) Discharging only dataset, (C) Combined dataset.

Figure 4 displays the average CA scores of each batch from the RNN + CA + 1D CNN and RNN + TA + CA + 1D CNN (SHA). In those figures, the x-axis represents the key, and the y-axis represents the query. Batches 1 and 3, sharing similar charging and rest policies, exhibit comparable CA score patterns for both models. In contrast, Batch 2 displays slightly different patterns. Two weaknesses are identified for the RNN + CA + 1D CNN model compared to the RNN + TA + CA + 1D CNN model. Firstly, owing to the vulnerability of RNN + CA + 1D CNN to VG-induced degradation, the context vector of each cycle fails to represent cycle information fully. Consequently, crucial key cycles (indicating high attention scores for nearly all queries) cannot be identified for the RNN + CA + 1D CNN model, hindering the potential reduction of input dimension (Figure 4A).

For RNN + TA + CA + 1D CNN (SHA), the disparity in CA scores between Batches 1, 3 and Batch 2 is more pronounced than in RNN + CA + 1D CNN (Figure 4B). Consequently, the potential to reduce the input dimension based on crucial key cycles is more evident. In Batches 1 and 3, cycles 20-40 and 85-90 emerge as crucial key cycles for regression, with minimal attention given to cycles 60-80. Conversely, Batch 2 places the highest importance on cycles 60-80 in Batch 2. This aligns with the substantial weights assigned to the rest period between cycles 60-80, as depicted in Figure 3C. Thus, we conclude that the rest time significantly influences the determination of cycles crucial for the regression.

The impact of multi-heads for CA is analyzed in Figure 5, illustrating the CA score patterns from the RNN + TA + CA + 1D CNN model with five heads. Similar to previous observations, the patterns of Batch 2 significantly differ from those of Batches 1 and 3; notably, patterns of heads 2, 4 and 5

exhibit considerable similarity, suggesting redundancy. Consequently, adding more heads beyond 3 harms performance, introducing unnecessary complexity and complicating the training process. Detailed results for various numbers of heads can be found in the Supplementary Information (Figure S3-5). For all the batches, cycles 0-20 are identified as significant, as captured by heads 1 and 2. This contrasts with the SHA case, where these cycles did not receive attention. Considering that significant cycles range from cycle 60-80 (Batch 2, SHA as CA; Batches 1, 3, Head 1 of MHA as CA) 20-40 (Batches 1, 3, SHA as CA; Batch 2, Head 1 of MHA as CA; Batches 1 to 3, Head 3 of MHA as CA), and 0-20 (Batches 1, 3, Head 1 of MHA as CA) in RNN + TA + CA + 1D CNN-based results, 80, 50, 30 are selected as the number of necessary input cycles to predict knee-onset.



**Figure 4. Average CA scores from RNN + CA + 1D CNN and RNN + TA + CA + 1D CNN (SHA).**  
 (A) RNN + CA + 1D CNN, (B) RNN + TA + CA + 1D CNN (SHA).

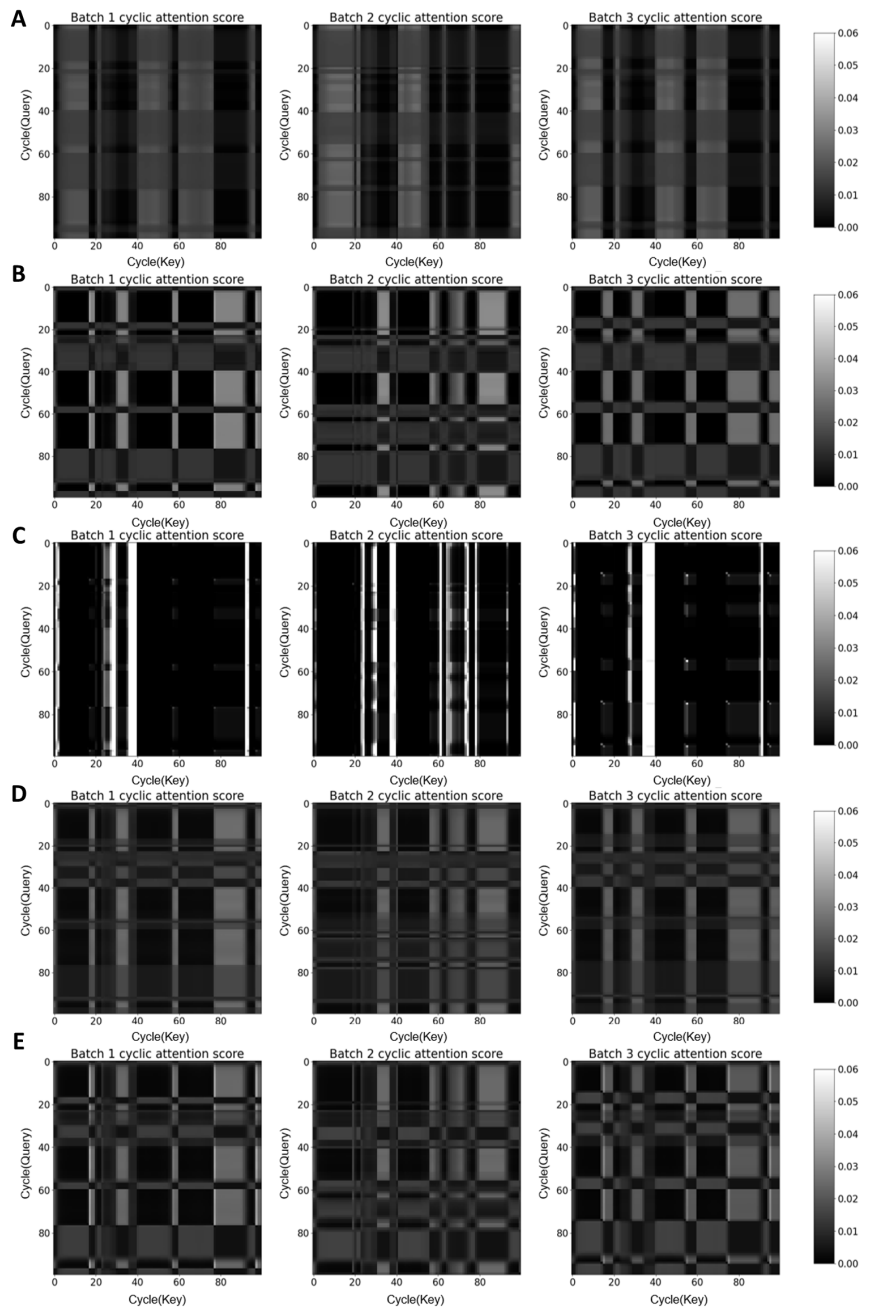


**Figure 5. CA scores from RNN + TA + CA + 1D CNN with five heads. (A) Head 1, (B) Head 2, (C) Head 3, (D) Head 4, (E) Head 5.**

## Input reduction scenario

The study showed that crucial information for the knee-onset prediction could be extracted from a subset of the initial 100 cycles. Moreover, important cycles vary for each batch and change with the number of heads used for SA. In this subsection, we present the results of the input reduction test, where the determination of the number of cycles to include in the input data is based on the SA scores. For this test, RNN + TA + CA + 1D CNN is trained with SHA and MHA for CA for comparison purposes. The head size for MHA was fixed at 3, as determined from the results of the 100-cycle regression test.

**Table 2** compares the results of the input reduction test when SHA and MHA are employed for CA in the RNN + TA + CA + 1D CNN. First, we successfully decreased the input dimension to 50 cycles with SHA for CA. The regression performance experienced only a slight degradation when the input size was reduced to 80 and 50 cycles, compared to the 100-cycle scenario. However, a more pronounced increase in error was observed when the input size was further reduced to 30 cycles.

MHA-based CA consistently exhibited superior regression performance compared to SHA in all cases, particularly when 30 cycles were used as input. As shown in the previous section, the MHA-based CA consistently outperformed SHA-based CA in all tests, especially when selecting an appropriate number of heads. Notably, the increase in test loss with 30 cycles as input was much less for the MHA case. The test error for the input of 30 cycles was nearly identical to that for 100 cycles, indicating the potential of a substantial reduction in input dimension without sacrificing performance.

Furthermore, input reduction results of all datasets can be better understood by comparing the results from using each batch separately, as summarized in **Table 2** and **Figure S8B-D**. As we conducted with all batches at once, each batch's regression results are tested with SHA- and MHA-based CA again. To recap, the cells in Batch 2 have an increased IR due to the extended rest period and thus experience much faster knee-onset than those in the other batches. Also, the lifespan distribution of cells in this batch is much more uniform than those in Batches 1 and 3. Therefore, regardless of which algorithm is used, the average error is the lowest in Batch 2.

With this knowledge, the SHA-based CA results are discussed first. Although the average test error in Batch 2 increases when the input is reduced by 50 cycles, it does not significantly impact the overall performance because the range of test loss is much smaller than in the other batches. Instead, since Batch 1 has a high cyclic attention score between cycles 30 and 40, as in **Figure 4B**, a large increase in error is observed for Batch 1 when the input is reduced to 30 cycles. This change also leads to a significant error for all the batches when the input is reduced to 30 cycles.

Using MHA can help cope with this problem. In **Figure 5**, we can see that the MHA judges the information in cycles 0-20 to be important in some heads. This modest increase in degrees of freedom due to the increased heads led to performance improvements when the number of input cycles was reduced to 30.

Detailed results when MHA-based CA is used for each batch are discussed as follows. Regardless of batch or number of input cycles, the MHA-based CA shows better (or at least similar) results than the SHA-based CA. Especially for Batch 1, the MHA-based CA gives good regression performance even when only 30 cycles are used as input. This can be explained as the MHA-based CA captures cycles before cycle 30 as having important information, as shown in **Figure 5**. For Batch 3, where complex charging strategies are employed, the regression results show that the MHA-based CA reduces the error for knee-onset by more than ten cycles in all experiments. When the input is 30 cycles, the difference between the SHA-based CA and the MHA-based CA becomes about 15 cycles.

To conclude, MHA-based CA (compared to SHA-based CA) reduced test loss meaningfully for Batches 1 and 3 when the input dataset is reduced. MHA-based CA reduced the requisite input cycle

number to 30 cycles when the data from all batches were used together.

**Table 2.** Input reduction results for RNN + TA + CA + 1D CNN trained with all batches, batch 1, batch 2, and batch 3. For MHA, 3 heads are used.

Test loss (RMSE)		100 cycles	80 cycles	50 cycles	30 cycles
All batches	SHA	60.71	59.49	59.79	76.52
	MHA	<b>56.20</b>	<b>57.01</b>	<b>55.61</b>	<b>58.56</b>
Batch 1	SHA	29.42	29.73	34.16	67.36
	MHA	<b>26.47</b>	<b>29.29</b>	<b>30.53</b>	<b>30.89</b>
Batch 2	SHA	17.90	<b>15.02</b>	19.86	21.16
	MHA	<b>13.10</b>	15.80	<b>14.14</b>	<b>16.15</b>
Batch 3	SHA	67.49	68.63	69.27	76.13
	MHA	<b>59.44</b>	<b>57.98</b>	<b>59.33</b>	<b>61.04</b>

## Conclusion

In this paper, attention mechanisms, specifically TA and SA, are employed to develop and compare three distinct data-driven models for LIB lifespan prediction: RNN + TA + 1D CNN, RNN + CA + 1D CNN, and RNN + TA + CA + 1D CNN. These proposed models use easily measurable variables as input, such as voltage, current, temperature, and capacity. Additionally, information during the rest phase is incorporated as an indirect measure of internal resistance, which is known to exhibit a significant correlation with lifespan.

The introduction of TA notably improved the performance of the baseline RNN + 1D CNN model, primarily due to its capability to mitigate the VG problem. Particularly, for Batch 2, which has the longest rest time, it was observed that high TA scores were assigned to certain rest phases, underscoring the significance of rest time in lifespan prediction. Given the similarities between Batches 1 and 3 and their distinctions with Batch 2, the RNN + CA + 1D CNN model highlighted similar key factors for Batch 1 and 3 while indicating different keys as important for Batch 2.

The RNN + TA + CA + 1D CNN model showed superior performance among all models, benefitting from the evident synergy between TA and SA. The SA score patterns obtained were entirely distinct from those of the RNN + CA + 1D CNN model, allowing for clear identification of crucial cycles. Notably, the CA scores for Batch 2 exhibited significant deviations from those of Batches 1 and 3. The enhanced performance of this model is attributed to the absence of VG issues, indicating the potential for reducing input dimension. Furthermore, the effectiveness of MHA was tested. Initially, having more heads for SA improved performance, but beyond three, adding more heads became detrimental, increasing model complexity without extracting additional information.

We also conducted an input reduction test based on the SA scores extracted from the RNN + TA + CA + 1D CNN model. When the data from all the batches were used for training with SHA, we successfully reduced the input dimension to 50 cycles (from 100 cycles) with minimal loss in performance. The input dimension could be reduced more effectively when MHA was employed (reduced to 30 cycles in all cases), with Batches 1 and 3 benefitting the most.

In summary, attention mechanisms prove beneficial for capturing crucial time and cycle information from a cycling dataset for LIB model prediction. This application improves performance by mitigating the VG effect and simplifies the model by reducing the input requirements.

# Experimental Procedures

## Resource Availability

## Lead Contact

Further information and requests for resources and materials should be directed to and will be fulfilled by the Lead Conatct, Jay H. Lee ([jlee4140@usc.edu](mailto:jlee4140@usc.edu)).

## Materials Availability

This study did not generate new unique reagents.

## Data and Code availability

Severson dataset can be accessed at <https://data.matr.io/1/projects/5c48dd2bc625d700019f3204>. The codes used in this work based on the Severson dataset, implementing RNN + TA + 1D CNN, RNN + CA + 1D CNN, and RNN + TA + CA + 1D CNN with SHA and MHA for CA, plotting temporal and cyclic attention scores, and the input reduction tests based on the cyclic attention scores, can be found [https://github.com/Jaewook-L/Temporal\\_Cyclic-attention](https://github.com/Jaewook-L/Temporal_Cyclic-attention).

## Input and output formulation

The primary goal of this study is to devise a machine-learning technique that efficiently utilizes readily available information from a relatively small number of initial charge and/or discharge cycles of LIBs to predict their lifespan. Our specific aim is to predict *knee-onset*, which signifies the initiation of nonlinear capacity degradation, utilizing data from a fixed number of initial cycles. Knee-onset can be estimated from the capacity degradation curve with the double Bacon-Watts model outlined below:

$$Q = \alpha_0 + \alpha_1(c - c_{k0}) + \alpha_2(c - c_{k0}) \tanh\{(c - c_{k0})/\gamma\} + \alpha_3(c - c_{2nd}) \tanh\{(c - c_{2nd})/\gamma\} + Z \quad (1)$$

where  $Q$  represents the capacity,  $c$  denotes the cycle number,  $c_{k0}$  is the knee-onset,  $c_{2nd}$  is the second transition point,  $\alpha_1, \alpha_2$  and  $\alpha_3$  are the model parameters to be estimated,  $\gamma$  is an adjustable parameter, and  $Z$  is a white noise<sup>33</sup>. It is well-established that internal resistance (IR) increases significantly after the knee-onset, leading to nonlinear degradation behavior<sup>34</sup>. The knee-onset of some cells is illustrated in [Figure S1](#), and detailed values for each cell are provided in [Table S1](#).

The input variables include voltage ( $V$ ), current ( $I$ ), temperature ( $T$ ), charging capacity ( $Q_c$ ) and discharging capacity ( $Q_d$ ). For a variable  $var$ ,  $var_{c_j, t_i}^{ce_m}$  represents its value at time  $t_i$  of cycle  $c_j$  (cell  $ce_m$ ). Let  $n_{cy}$  and  $n_{ts}$  be the number of input cycles used and the total number of time steps per cycle, respectively. The input data matrix  $\mathbf{X}^{ce_m}$  can be formed for cell  $ce_m$  can then be formulated as follows:

$$\mathbf{X}^{ce_m} = \begin{bmatrix} V_{1,1}^{ce_m} & \dots & V_{1,n_{ts}}^{ce_m} & \dots & \dots & V_{n_{cy},1}^{ce_m} & \dots & V_{n_{cy},n_{ts}}^{ce_m} \\ I_{1,1}^{ce_m} & \dots & I_{1,n_{ts}}^{ce_m} & \dots & \dots & I_{n_{cy},1}^{ce_m} & \dots & I_{n_{cy},n_{ts}}^{ce_m} \\ T_{1,1}^{ce_m} & \dots & T_{1,n_{ts}}^{ce_m} & \dots & \dots & T_{n_{cy},1}^{ce_m} & \dots & T_{n_{cy},n_{ts}}^{ce_m} \\ Q_{c1,1}^{ce_m} & \dots & Q_{c1,n_{ts}}^{ce_m} & \dots & \dots & Q_{cn_{cy},1}^{ce_m} & \dots & Q_{cn_{cy},n_{ts}}^{ce_m} \\ Q_{d1,1}^{ce_m} & \dots & Q_{d1,n_{ts}}^{ce_m} & \dots & \dots & Q_{dn_{cy},1}^{ce_m} & \dots & Q_{dn_{cy},n_{ts}}^{ce_m} \end{bmatrix} \quad (2)$$

## Preprocessing, data split, and main hyperparameters

The Severson dataset includes some outliers, which are removed and replaced by extrapolated

values in alignment with Yang et al.<sup>35</sup>, and the noise level is reduced using the Savitzky-Golay filter<sup>36</sup>. Subsequently, min-max normalization is applied to scale the input values from 0 to 1. To ensure representative results (independent of random grouping), five distinct random selections of training, validation, and test sets are attempted, and their results are averaged.

For the dataset split, we randomly selected 80, 20, and 24 cells among the 124 cells, designating the corresponding data sets as training, validation, and test sets. To assess the impact of initialization, we employed five different splits of training, validation, and test sets generated by different random seeds. We calculated the average and standard deviation of the test losses. The error bars of test loss, computed from the results of five different seeds, are presented in [Figure S6, S7, and S9](#), demonstrating the consistency of the model's performance concerning the initialization.

Based on the outcomes of preliminary tests involving multiple RNN types, GRU was selected as the RNN type. To counteract overfitting, early stopping was implemented, where [epoch, patience] was set to [3000, 500] for training using data from all the batches and [1000, 10] for training with data from each batch, respectively. Regarding MHA, the number of heads varied from 1 to 5, and the detailed hyperparameter values we settled on are provided in [Table S6-S10](#).

### Baseline models from our previous work

[Figure 6](#) illustrates the data-driven models used in our previous work<sup>17</sup>, which will serve as the starting points for the models developed in this study. Two constituents of these models are CNN and RNN. CNN, a neural network type designed for extracting spatially local features through convolution kernels<sup>37</sup>, is combined with RNN, widely used for time series modeling, where the outputs of the hidden states serve as inputs to the same nodes for subsequent time step calculations.

In the case of CNN, the limited span of the kernel used<sup>38</sup> necessitates many layers to effectively extract information regarding the entire cycle, potentially causing the vanishing gradient (VG) problem. In our earlier work, we proposed two data-driven models, namely RNN + 1D CNN and RNN + 2D CNN<sup>17</sup>, by integrating RNN with CNN. In RNN + 1D CNN, the last hidden states of the RNN are used as inputs to the 1D CNN. Incorporating RNN to encode input information reduced the layer depth of the CNN and training time. However, the VG problem persisted as the time series of a cycle could be a long sequence.

In RNN + 2D CNN, the entire sequence of hidden states from the RNN is used as inputs to the 2D CNN. This model helped mitigate the VG problem and enhance accuracy, albeit with a longer training time. The major drawback of RNN + 2D CNN lies in its high memory requirements and training difficulty, which can become pronounced with increasing data sampling rates or decreasing charging rates.

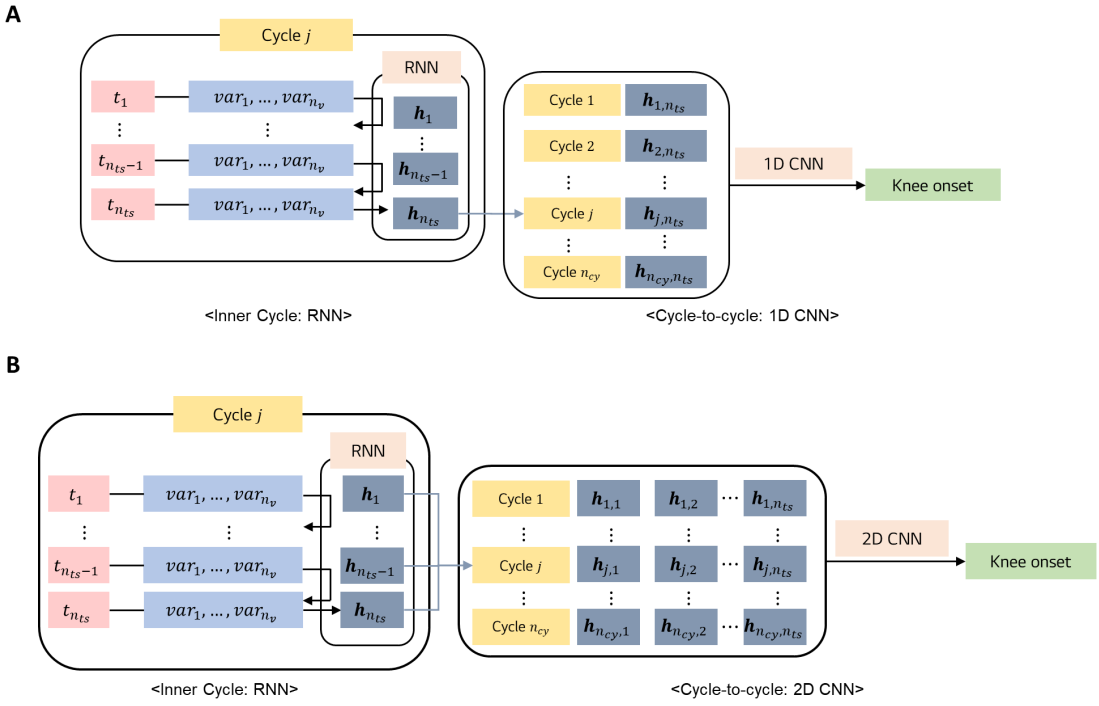


**Figure 6. RNN-CNN based models from our previous work. (A) RNN + 1D CNN model, (B) RNN + 2D CNN model.**

### Temporal attention

TA is an attention-based algorithm commonly applied to sequential data, such as those in NLP and time-series modeling. TA functions by assigning varying weights to previous inputs based on their influence in generating the output of a desired sequence. Using these weighted inputs, a *context vector* is calculated, flexibly reflecting the impact of previous inputs. The TA score for each element of the sequence indicates its importance. It is worth noting that although it is possible to use non-RNN models, such as feedforward neural networks, for sequential data, this is beyond the scope of our study.

When TA is integrated with RNNs, the hidden states serve as inputs to the TA layer. We focus on TA for multi-input-single-output (MISO) cases as the output has a scalar value (knee-onset in our case). The two main equations used to calculate the TA score of a hidden state of time step  $t_i$  in an RNN-based MISO problem are shown below.

$$\alpha_i = \text{const.} \quad (3)$$

$$\alpha_i = \frac{\exp(\mathbf{w}_b \mathbf{h}_i^T)}{\sum_{i=1}^{n_{ts}} \exp(\mathbf{w}_b \mathbf{h}_i^T)} \quad (4)$$

Eq. (3) fixes the attention score at each time step  $t_i$  to a constant value, which is simple and meaningful if the relationship between time steps is consistent throughout the input data. However, it is unsuitable in our case due to different cells employing distinct charging and resting strategies, leading to dynamically changing relative importance of time steps.

Eq. (4) keeps the weight vector  $\mathbf{w}_b$  fixed during training but adjusts a TA score based on the incoming hidden state. Since the importance of a time step can be set differently depending on the value of the hidden state, it allows for variations in the importance of time steps in dynamic data. Note that, as the hidden state is also a result of the learned RNN layer, training should be conducted to ensure that the calculated attention output accurately reflects the importance. Details of TA with dynamic attention

scores are depicted in Figure 7. After calculating the refined hidden state  $\tilde{\mathbf{h}}_i = \mathbf{w}_b \mathbf{h}_i^T$  from each hidden state  $\mathbf{h}_i$ , the TA score from each time step is calculated from the refined hidden state and multiplied to each hidden state.

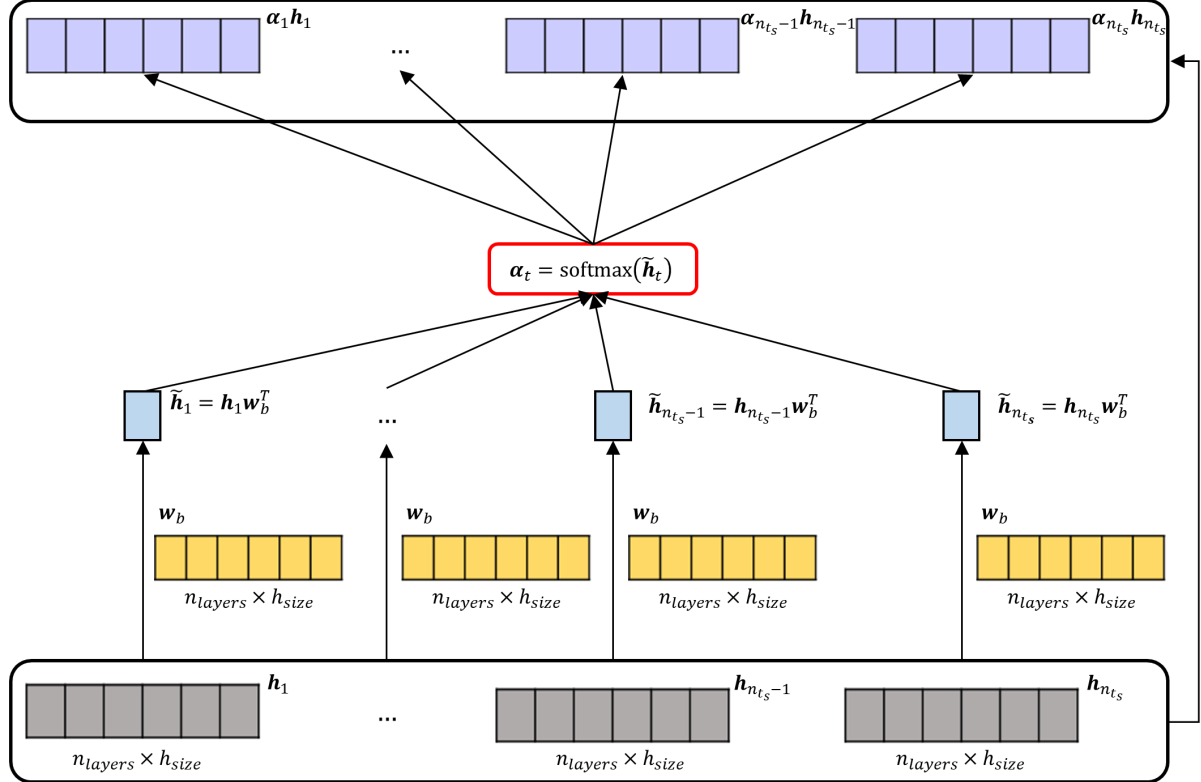


**Figure 7. Schematic of temporal attention with dynamic attention scores.** Represented by Eq. (4),  $n_{layers}$  refers to the number of RNN layers,  $h_{size}$  refers to the size of each hidden state. In this approach, we used only  $n_{layer} = 1$ .

### Self-Attention

SA is a recently proposed attention mechanism in Transformer architectures<sup>19</sup>, and its application to various NLP problems, as demonstrated in Devlin et al.<sup>39</sup> has garnered significant attention. In the Transformer framework, SA estimates relationships between different positions within a given sequence. When used with RNN, SA utilizes the similarity among hidden states to give higher weights to more representative hidden states. SA introduces three concepts to calculate the attention score: *query*, *key*, and *value*. Further details about each concept can be found in Niu et al.<sup>40</sup>.

SA can extract key representative features of cycle-to-cycle behavior for cyclic datasets based on cycles' similarities. In the knee-onset prediction problem, this can aid in reducing the number of input cycles: If a specific cycle already possesses much information from other future cycles in the input, then the input to predict knee-onset can be effectively reduced to that specific cycle. In our problem, inputs for the SA are computed from the hidden states of each cycle, referred to as the context vectors (denoted as  $\mathbf{ct}$  for the sake of our discussion below).

Let the current cycle be  $c_j$  among  $n_{cy}$  cycles. The similarity between the context vectors from the RNN at  $c_j$ ,  $\mathbf{ct}_j$  and that at another cycle  $c_{j'}$ ,  $\mathbf{ct}_{j'}$  can be measured by SA. In this case, query ( $\mathbf{q}$ ) is the vector encoding  $\mathbf{ct}_j$  and key ( $\mathbf{k}$ ) is the vector encoding  $\mathbf{ct}_{j'}$ . Value ( $\mathbf{v}$ ) is a vector representing the actual context vector associated with the key, i.e.,  $\mathbf{ct}_{j'}$ . Additionally, let the size of the input

originally belonging to each sequence be  $d_{model}$ , and the size of the query, key, and value  $d_q, d_k, d_v$ . In SA,  $d_q, d_k, d_v$  are all equal.

We multiply the encoded query and key to calculate the similarity between the two targets, which is the SA score. As the size of the key increases, the similarity between each variable weakens. To counteract this, we divide it by  $\sqrt{d_k}$  and apply the softmax function to normalize it to a value between 0 and 1. In this context,  $\text{softmax}\left(\frac{\mathbf{q}\mathbf{k}^T}{\sqrt{d_k}}\right)$  can be called the SA score for cycles  $c_j$  and  $c_{j'}$ . Finally, the value vector is multiplied by the SA score to compute the actual output of each target associated with the query, which is the final output of the SA. If we extend this calculation to the entire input matrix  $\mathbf{X}$  and denote the query, key, and value of  $\mathbf{X}$  as  $\mathbf{Q}, \mathbf{K}, \mathbf{V}$ , we can calculate the SA score matrix  $\mathbf{AS}$ , as shown in Eq. (4). A detailed schematic of the SA is presented in [Figure 8](#). For the output, the head of the SA layer is denoted as  $\mathbf{HE}$ .

Building on the key-query concept, we can attempt to reduce the input data size in predicting knee-onset as follows. The SA score of each query cycle is calculated for each key cycle. Then, suppose the SA score of a specific key cycle is consistently high across all query cycles. In that case, it indicates that the context vector of the key cycle already encapsulates crucial information representative of all the cycles. Consequently, the regression model can be constructed with only those cycles identified as important, presenting the potential to decrease the number of cycles needed to predict knee-onset.

$$\mathbf{Q} = \mathbf{X}\mathbf{W}^Q, \mathbf{K} = \mathbf{X}\mathbf{W}^K, \mathbf{V} = \mathbf{X}\mathbf{W}^V \quad (5)$$

$$\mathbf{HE} = \text{SelfAttention}(\mathbf{Q}, \mathbf{K}, \mathbf{V}) = \text{softmax}\left(\frac{\mathbf{Q}\mathbf{K}^T}{\sqrt{d_k}}\right)\mathbf{V} = \mathbf{ASV} \quad (6)$$

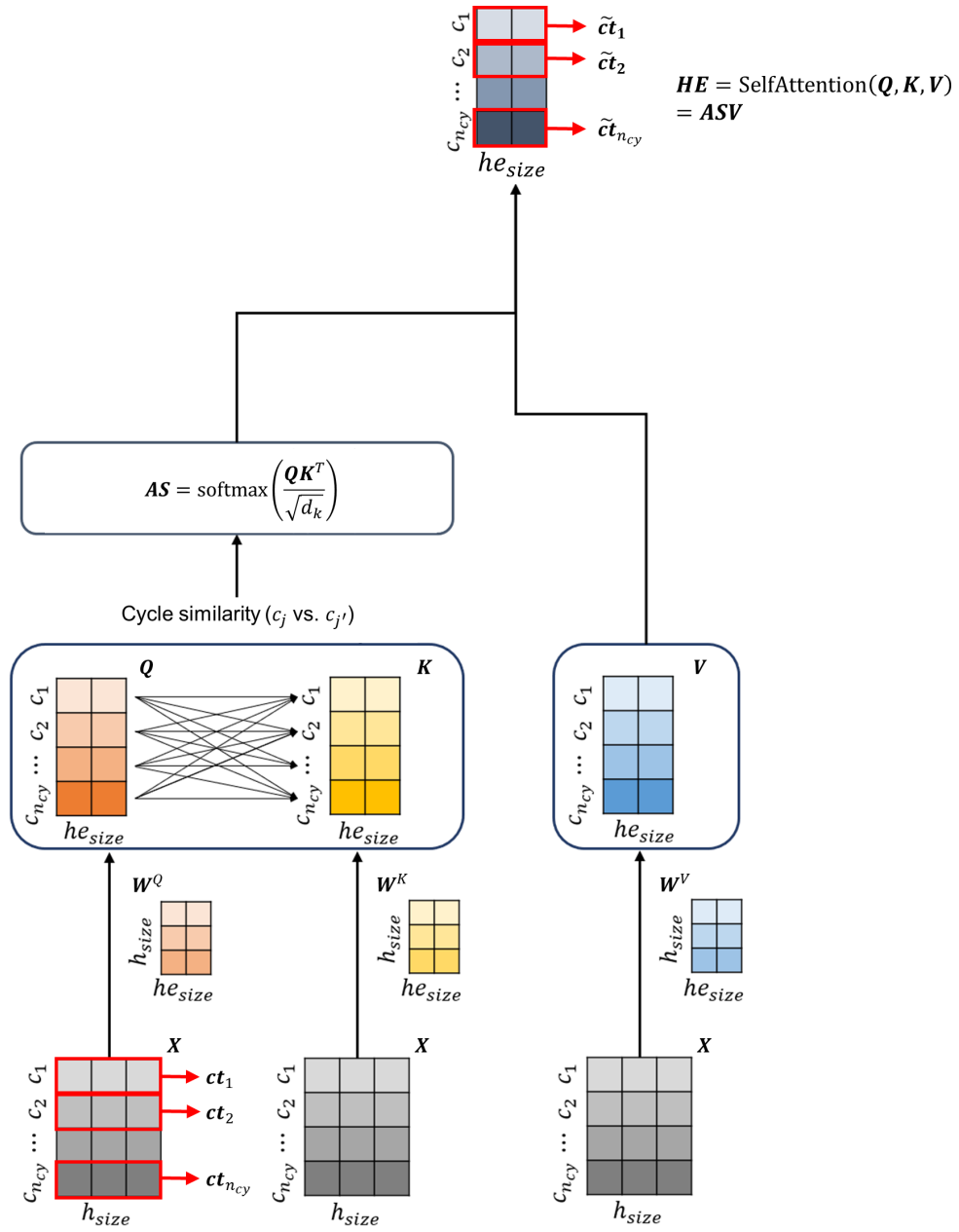


**Figure 8. Schematic of self-attention (SA).**  $he_{size}$  refers to the size of the head in the self-attention layer.

## Multi-head attention

A key advantage of CNN lies in its ability to utilize multiple kernels, enabling the examination of the same input from various perspectives. Different strides, kernel sizes, and dilations can be employed to explore the input data thoroughly, and the diverse information acquired from these different kernels can be concatenated to form a highly relevant output.

Multi-head attention (MHA) seeks to replicate the functionality of multiple feature maps in CNN by investigating input sequences from multiple viewpoints<sup>19</sup>. Although the receptive field of attention remains consistent across all inputs, MHA assigns distinct attention scores for different heads. Instead of designating a particular input as crucial, MHA allows the neural network to use diverse perspectives to assess the importance of each input. Like the multiple kernels in CNN, MHA has demonstrated its capability to enhance accuracy and stability compared to single-head attention (SHA).

In the knee-onset prediction problem, where inputs and outputs exhibit complex relationships, MHA could prove beneficial, as SHA may overlook some critical connections between inputs and outputs. With MHA, different input parts would be analyzed in diverse ways, reducing the likelihood of omitting essential information.

The mathematical representations of MHA are as follows. Although different inputs can be query and key/value for MHA, in our case, where MHA is combined with SA, all inputs for query, key, and value are denoted as  $\mathbf{X} \in \mathbf{R}^{n_{cy} \times d_{model}}$  ( $d_{model} = h_{size}$ ). Moreover, the sizes of query, key, and value are set equal in this approach, specifically  $d_q = d_k = d_v = h_{size}$ . The projection matrices for the  $p$ -th head are denoted as  $\mathbf{W}_p^Q \in \mathbf{R}^{d_{model} \times d_q}$ ,  $\mathbf{W}_p^K \in \mathbf{R}^{d_{model} \times d_k}$ , and  $\mathbf{W}_p^V \in \mathbf{R}^{d_{model} \times d_v}$ . Consequently, the query, key, and value matrices become  $\mathbf{Q}_p = \mathbf{X}\mathbf{W}_p^Q$ ,  $\mathbf{K}_p = \mathbf{X}\mathbf{W}_p^K$ ,  $\mathbf{V}_p = \mathbf{X}\mathbf{W}_p^V$ . After calculating the attention score  $\mathbf{AS}_p$  for each head using  $\text{softmax}\left(\frac{\mathbf{Q}_p \mathbf{K}_p^T}{\sqrt{d_k}}\right)$ , the output of each head  $\mathbf{HE}_p$  is calculated by multiplying  $\mathbf{AS}_p$  and  $\mathbf{V}_p$  as Eq. (7). Then, MHA can be performed by concatenating all the heads and multiplying the resulting matrix with  $\mathbf{W}^O \in \mathbf{R}^{d_v \times n_{he} d_v}$ , as shown in Eq. (8).

$$\mathbf{HE}_p = \text{SelfAttention}(\mathbf{Q}_p, \mathbf{K}_p, \mathbf{V}_p) = \text{softmax}\left(\frac{\mathbf{Q}_p \mathbf{K}_p^T}{\sqrt{d_k}}\right) \mathbf{V} = \mathbf{AS}_p \mathbf{V}_p \quad (7)$$

$$\text{MultiHead}(\mathbf{Q}, \mathbf{K}, \mathbf{V}) = \text{Concat}(\mathbf{HE}_1, \dots, \mathbf{HE}_{n_{he}})(\mathbf{W}^O)^T \quad (8)$$

Different weight matrices for each head are assigned to queries, keys, and values. The output of each head is then concatenated. To manage the output size, the matrix  $\mathbf{W}^O$  in the last step regulates the size as a simple concatenation of multiple heads' outputs could result in a large output size.

The Transformer architecture demonstrated that various heads produced distinct attention scores, allowing them to interpret complex sentences in multiple ways to uncover meaningful relationships. In our study, MHA is used with SA to identify important cycles, enabling the analysis of significant cycles from various perspectives based on similarities between context vectors of different cycles. If the regression model is appropriately trained, different heads capture diverse relationships between context vectors, thereby giving a more nuanced representation of the dataset. We analyzed the learned attention scores from each head to enhance regression performance and interpretability. Detailed steps of MHA are illustrated in [Figure 9](#).

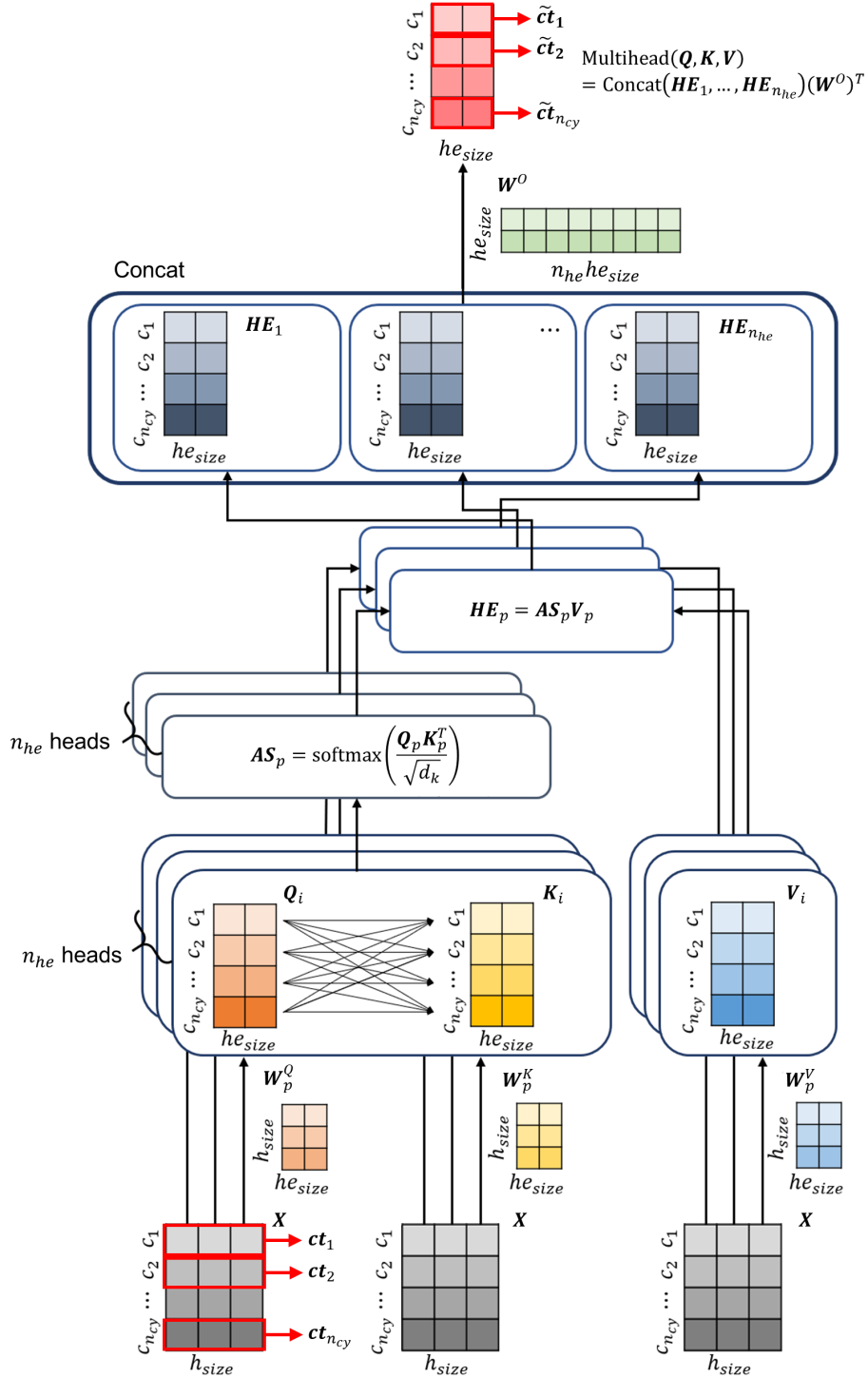


**Figure 9. Schematic of multi-head attention.**  $n_{he}$  refers to the number of heads.

## Acknowledgements

The authors thank Kristen. A. Severson and her colleagues for providing Severson dataset used in this study.

## Author Contributions

Conceptualization, J.L.; Methodology, J.L.; Software, J.L.; Formal Analysis, J.L.; Investigation,

J.L.; Visualization, J.L.; Writing-Original Draft, J.L.; Writing-Review & Editing, S.H. and J.H.L.; Supervision, J.H.L.

## **Declaration of Interests**

The authors declare no competing interests.

## Acronyms

1D CNN	one-dimensional convolutional neural network
2D CNN	two-dimensional convolutional neural network
AM	attention mechanism
BMS	battery management system
CA	cyclic attention
CC	constant current
CV	constant voltage
CNN	convolutional neural network
DHI	direct health index
EOL	end of life
EN	elastic net
EV	electric vehicle
GRU	gated recurrent unit
RNN	recurrent neural network
LIB	lithium ion battery
LSTM	long short-term memory
NLP	natural language processing
MHA	multi-head attention
MISO	multi-input single-output
OLS	ordinary least squares
RHI	refined health index
RMSE	root-mean-squared error
SA	self-attention
SEI	solid electrolyte interphase
SHA	single-head attention
SOC	state of charge
SOH	state of health
TA	temporal attention
VG	vanishing gradient
VIT	voltage, current, temperature

## Nomenclature

$t$	time step
$c$	cycle
$\mathbf{ct}$	context vector
$\tilde{\mathbf{ct}}$	refined context vector
$b$	batch
$ce$	cell
$he$	head
$\mathbf{AS}$	attention score matrix
$\mathbf{HE}$	head matrix
$t_i$	time step index
$c_j$	cycle index
$\mathbf{ct}_j$	context vector for cycle $c_j$
$b_l$	batch index
$ce_m$	cell index
$he_p$	head index
$\mathbf{AS}_p, \mathbf{HE}_p$	attention score, head matrix index for $he_n$
$c_{ko}$	knee-onset
$c_{2nd}$	2 <sup>nd</sup> transition point (cycle) from double Bacon-Watts model
$\alpha_1, \alpha_2, \alpha_3$	estimated model parameters of the double Bacon-Watts model
$\gamma, Z$	adjustable parameter and white noise of the double Bacon-Watts model
$V$	voltage (V)
$I$	current (A)
$T$	temperature (°C)
$Q$	capacity (Ah)
$var$	variable
$Q_c$	charging capacity (Ah)
$n_{cy}$	input cycle size
$\mathbf{X}$	input matrix for multi-head attention
$cr$	average C-rate
$cr_{1st}$	C-rate of the 1st charging step
$cr_{2nd}$	C-rate of the 2nd charging step
$n_{b_l}$	number of cells belonging to batch $b_l$
$Q_{tr}$	point of transition from the 1st to 2nd charging step (Ah)

$\alpha_i$	temporal attention score of $\mathbf{h}_i$
$\mathbf{h}$	hidden state vector
$\tilde{\mathbf{h}}_i$	refined hidden state vector
$\mathbf{w}_b$	weight vector of temporal attention
$n_{layers}$	number of RNN layers
$h_{size}$	size of each hidden state
$\mathbf{q}, \mathbf{k}, \mathbf{v}$	query, key, value vector encoded from the input vector
$\mathbf{Q}, \mathbf{K}, \mathbf{V}$	query, key, value matrix encoded from input matrix
$d_{model}$	input size
$d_q, d_k, d_v$	query, key, value size
$\mathbf{w}^Q, \mathbf{w}^K, \mathbf{w}^V$	weight vectors for input matrix to embed query, key, value
$\mathbf{W}^Q, \mathbf{W}^K, \mathbf{W}^V$	weight matrices for input matrix to embed query, key, value
$he_{size}$	each head's size
$n_{he}$	number of heads
$\mathbf{W}^O$	weight matrix to concatenated heads to single-head size
$n_v$	number of input variables
$Q_d$	discharging capacity
$n_{ts}$	number of time steps per cycle

## References

1. Wang, Y., Tian, J., Sun, Z., Wang, L., Xu, R., Li, M., and Chen, Z. (2020). A comprehensive review of battery modeling and state estimation approaches for advanced battery management systems. *Renewable and Sustainable Energy Reviews* 131, 110015.
2. Wu, Y., Wang, W., Ming, J., Li, M., Xie, L., He, X., Wang, J., Liang, S., and Wu, Y. (2019). An exploration of new energy storage system: high energy density, high safety, and fast charging lithium ion battery. *Advanced Functional Materials* 29, 1805978.
3. Chen, M., Ma, X., Chen, B., Arsenault, R., Karlson, P., Simon, N., and Wang, Y. (2019). Recycling end-of-life electric vehicle lithium-ion batteries. *Joule* 3, 2622-2646.
4. Kong, L., Li, C., Jiang, J., and Pecht, M.G. (2018). Li-ion battery fire hazards and safety strategies. *Energies* 11, 2191.
5. Han, X., Lu, L., Zheng, Y., Feng, X., Li, Z., Li, J., and Ouyang, M. (2019). A review on the key issues of the lithium ion battery degradation among the whole life cycle. *ETransportation* 1, 100005.
6. Xia, Z., and Qahouq, J.A.A. (2020). Evaluation of parameter variations of equivalent circuit model of lithium-ion battery under different SOH conditions. (IEEE), pp. 1519-1523.
7. Fuller, T.F., Doyle, M., and Newman, J. (1994). Simulation and optimization of the dual lithium ion insertion cell. *Journal of the electrochemical society* 141, 1.
8. Hu, X., Xu, L., Lin, X., and Pecht, M. (2020). Battery lifetime prognostics. *Joule* 4, 310-346.
9. Ng, M.-F., Zhao, J., Yan, Q., Conduit, G.J., and Seh, Z.W. (2020). Predicting the state of charge and health of batteries using data-driven machine learning. *Nature Machine Intelligence* 2, 161-170.
10. Severson, K.A., Attia, P.M., Jin, N., Perkins, N., Jiang, B., Yang, Z., Chen, M.H., Aykol, M., Herring, P.K., and Fragedakis, D. (2019). Data-driven prediction of battery cycle life before capacity degradation. *Nature Energy* 4, 383-391.
11. Richardson, R.R., Osborne, M.A., and Howey, D.A. (2017). Gaussian process regression for forecasting battery state of health. *Journal of Power Sources* 357, 209-219.
12. Nuhic, A., Terzimehic, T., Soczka-Guth, T., Buchholz, M., and Dietmayer, K. (2013). Health diagnosis and remaining useful life prognostics of lithium-ion batteries using data-driven methods. *Journal of power sources* 239, 680-688.
13. Ren, L., Dong, J., Wang, X., Meng, Z., Zhao, L., and Deen, M.J. (2020). A data-driven auto-CNN-LSTM prediction model for lithium-ion battery remaining useful life. *IEEE Transactions on Industrial Informatics* 17, 3478-3487.
14. Zraibi, B., Okar, C., Chaoui, H., and Mansouri, M. (2021). Remaining useful life assessment for lithium-ion batteries using CNN-LSTM-DNN hybrid method. *IEEE Transactions on Vehicular Technology* 70, 4252-4261.
15. Roman, D., Saxena, S., Robu, V., Pecht, M., and Flynn, D. (2021). Machine learning pipeline for battery state-of-health estimation. *Nature Machine Intelligence* 3, 447-456.
16. Lin, C., Xu, J., Hou, J., Liang, Y., and Mei, X. (2023). Ensemble method with heterogeneous models for battery state-of-health estimation. *IEEE Transactions on Industrial Informatics*.
17. Lee, J., and Lee, J.H. (2024). Simultaneous extraction of intra-and inter-cycle features for predicting lithium-ion battery's knees using convolutional and recurrent neural networks. *Applied Energy* 356, 122399.
18. Cho, K., Van Merriënboer, B., Bahdanau, D., and Bengio, Y. (2014). On the properties of neural machine translation: Encoder-decoder approaches.
19. Vaswani, A., Shazeer, N., Parmar, N., Uszkoreit, J., Jones, L., Gomez, A.N., Kaiser, Ł., and Polosukhin, I. (2017). Attention is all you need.
20. You, Q., Jin, H., Wang, Z., Fang, C., and Luo, J. (2016). Image captioning with semantic attention. pp. 4651-4659.
21. Lee, K.-H., Chen, X., Hua, G., Hu, H., and He, X. (2018). Stacked cross attention for image-text matching. pp. 201-216.
22. Du, S., Li, T., Yang, Y., and Horng, S.-J. (2020). Multivariate time series forecasting via attention-based encoder-decoder framework. *Neurocomputing* 388, 269-279.
23. Zhang, B., Zou, G., Qin, D., Lu, Y., Jin, Y., and Wang, H. (2021). A novel Encoder-Decoder model based on read-first LSTM for air pollutant prediction. *Science of the Total Environment* 765,

144507.

24. Wang, F., and Tax, D.M. (2016). Survey on the attention based RNN model and its applications in computer vision.
25. Yang, K., Tang, Y., Zhang, S., and Zhang, Z. (2022). A deep learning approach to state of charge estimation of lithium-ion batteries based on dual-stage attention mechanism. *Energy* 244, 123233.
26. Hochreiter, S., and Schmidhuber, J. (1997). Long short-term memory. *Neural computation* 9, 1735-1780.
27. Cho, K., Van Merriënboer, B., Gulcehre, C., Bahdanau, D., Bougares, F., Schwenk, H., and Bengio, Y. (2014). Learning phrase representations using RNN encoder-decoder for statistical machine translation.
28. Zhao, H., Chen, Z., Shu, X., Shen, J., Lei, Z., and Zhang, Y. (2023). State of health estimation for lithium-ion batteries based on hybrid attention and deep learning. *Reliability Engineering & System Safety* 232, 109066.
29. Jiang, Y., Chen, Y., Yang, F., and Peng, W. (2023). State of health estimation of lithium-ion battery with automatic feature extraction and self-attention learning mechanism. *Journal of Power Sources* 556, 232466.
30. Wei, Y., and Wu, D. (2023). Prediction of state of health and remaining useful life of lithium-ion battery using graph convolutional network with dual attention mechanisms. *Reliability Engineering & System Safety* 230, 108947.
31. Xiong, W., Xu, G., Li, Y., Zhang, F., Ye, P., and Li, B. (2023). Early prediction of lithium-ion battery cycle life based on voltage-capacity discharge curves. *Journal of Energy Storage* 62, 106790.
32. Lee, J., and Lee, J.H. (2023). Simultaneous Feature Extraction of Intra-and Inter-Cycle Changes for Knee Point Prediction of Lithium Ion Batteries. *IFAC-PapersOnLine* 56, 4639-4644.
33. Fermín-Cueto, P., McTurk, E., Allerhand, M., Medina-Lopez, E., Anjos, M.F., Sylvester, J., and dos Reis, G. (2020). Identification and machine learning prediction of knee-point and knee-onset in capacity degradation curves of lithium-ion cells. *Energy and AI* 1, 100006.
34. Schuster, S.F., Bach, T., Fleder, E., Müller, J., Brand, M., Sextl, G., and Jossen, A. (2015). Nonlinear aging characteristics of lithium-ion cells under different operational conditions. *Journal of Energy Storage* 1, 44-53.
35. Yang, Y. (2021). A machine-learning prediction method of lithium-ion battery life based on charge process for different applications. *Applied Energy* 292, 116897.
36. Schafer, R.W. (2011). What is a Savitzky-Golay filter? [lecture notes]. *IEEE Signal processing magazine* 28, 111-117.
37. LeCun, Y., Bottou, L., Bengio, Y., and Haffner, P. (1998). Gradient-based learning applied to document recognition. *Proceedings of the IEEE* 86, 2278-2324.
38. Agrawal, A., and Mittal, N. (2020). Using CNN for facial expression recognition: a study of the effects of kernel size and number of filters on accuracy. *The Visual Computer* 36, 405-412.
39. Devlin, J., Chang, M.-W., Lee, K., and Toutanova, K. (2018). Bert: Pre-training of deep bidirectional transformers for language understanding.
40. Niu, Z., Zhong, G., and Yu, H. (2021). A review on the attention mechanism of deep learning. *Neurocomputing* 452, 48-62.

**Supplementary Information for  
Attention Mechanism for Lithium-Ion Battery Lifespan Prediction:  
Temporal and Cyclic Attention**

**Jaewook Lee<sup>1</sup>, Seongmin Heo<sup>1</sup>, Jay H. Lee<sup>1, 2, 3,\*</sup>**

<sup>1</sup> *Department of Chemical and Biomolecular Engineering, Korea Advanced Institute of Science and Technology, 291 Daehak-ro, Yuseong-gu, Daejeon 34141, Republic of Korea*

<sup>2</sup> *Mork Family Department of Chemical Engineering and Materials Science, University of Southern California, 3651 Watt Way, Los Angeles, CA 90089, United States*

<sup>3</sup> *Lead Contact*

*\* Correspondence. E-mail address: [jlee4140@usc.edu](mailto:jlee4140@usc.edu) (J.H. Lee).*

## Supplementary Figures

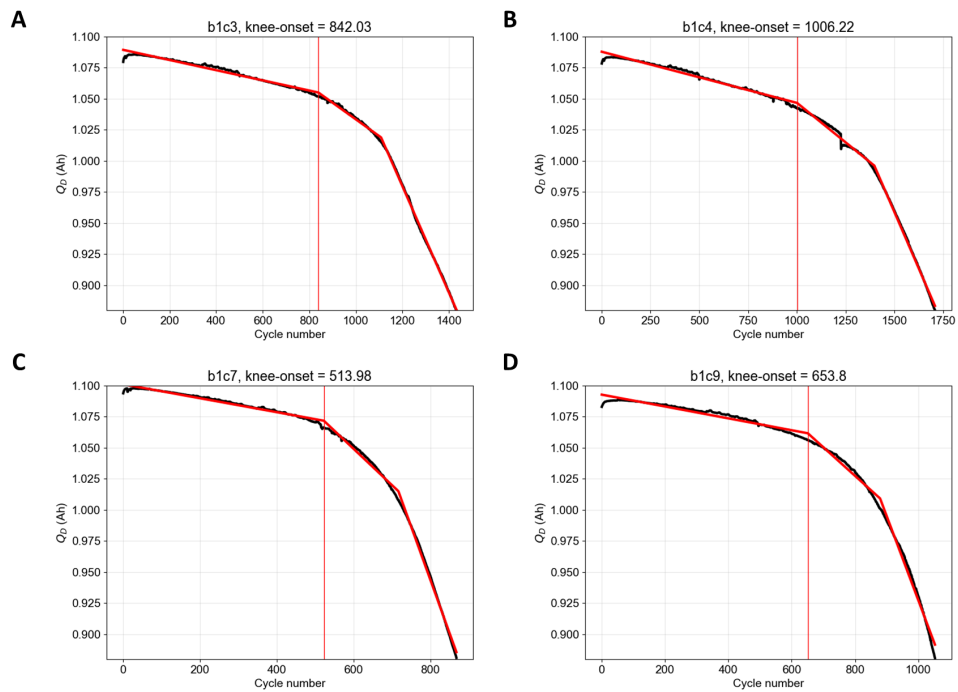
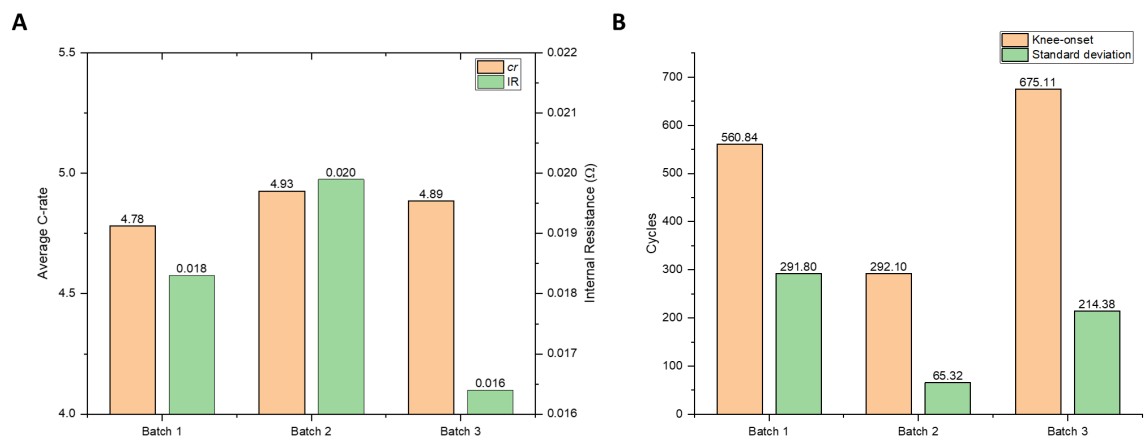
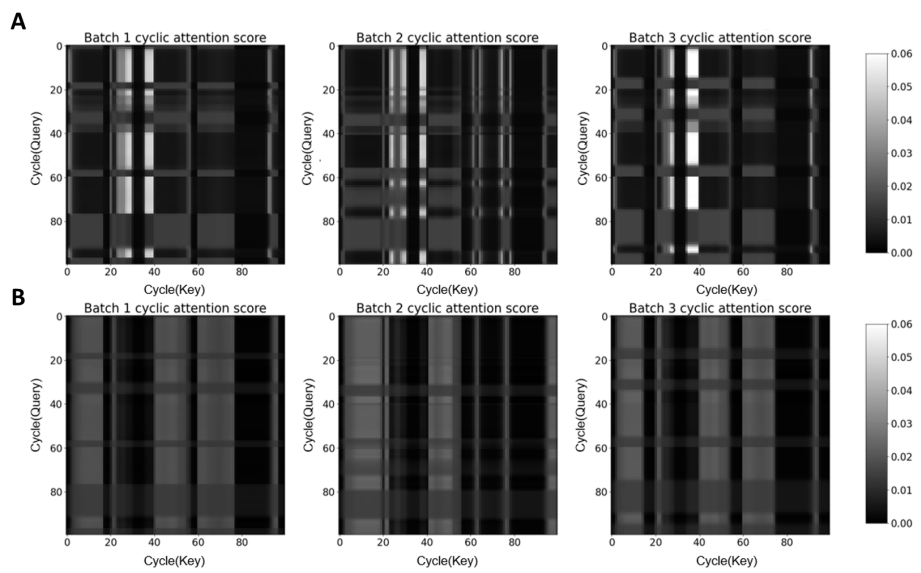


Figure S1. **Knee-onset of some selected cells.** (A) b1c3. (B) b1c4, (C) b1c7, (D) b1c9.



**Figure S2. Different operating conditions and lifespans for each batch.** (A) Average C-rate, IR (last 100 cycles) for each batch. (B) Average and standard deviation of knee-onset for each batch.



**Figure S3. CA scores from RNN + TA + CA + 1D CNN for 100 cycles as input with two heads. (A) Head 1, (B) Head 2.**

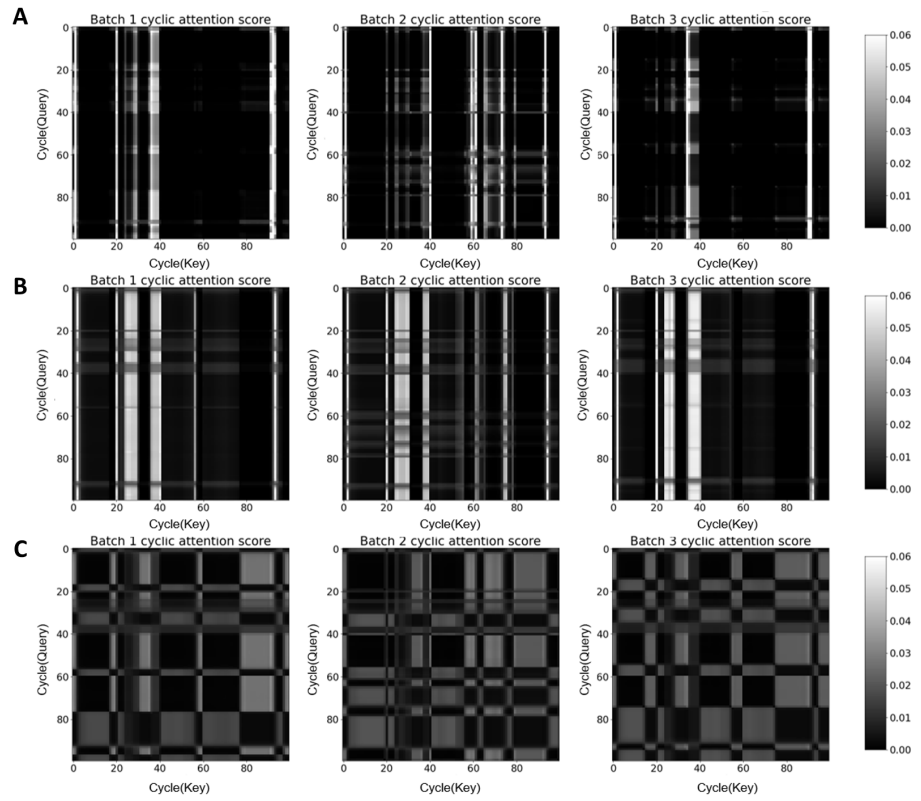


**Figure S4. Scores from RNN + TA + CA + 1D CNN for 100 cycles as input with three heads. (A) Head 1, (B) Head 2, (C) Head 3.**

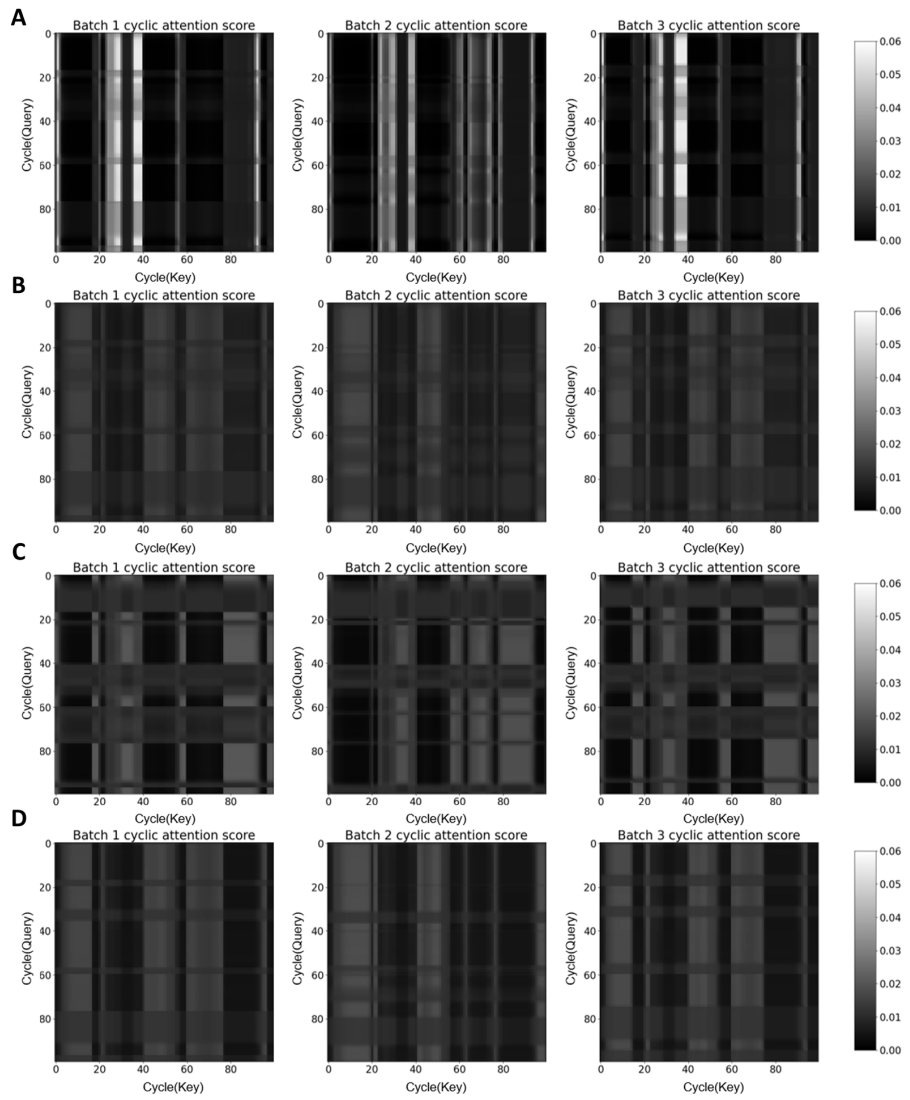


**Figure S5. CA scores from RNN + TA + CA + 1D CNN for 100 cycles as input with four heads. (A) Head 1, (B) Head 2, (C) Head 3, (D) Head 4.**

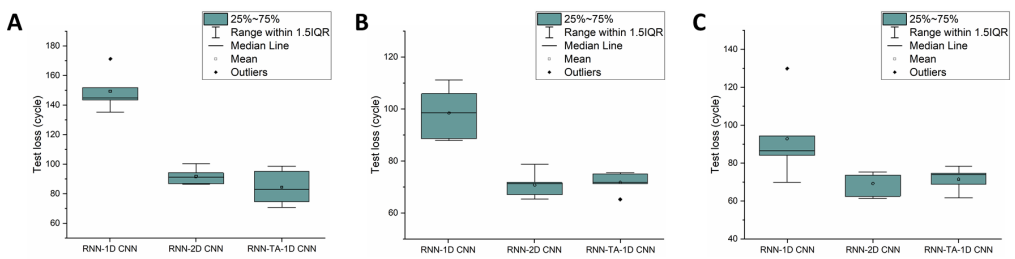


**Figure S6. Losses with error bars for RNN + 1D CNN, RNN + 2D CNN, and RNN + TA + 1D CNN with best hyperparameter values when three different datasets are used with five random seeds. (A) Charging data only, (B) Discharging data only, (C) Combined dataset.**

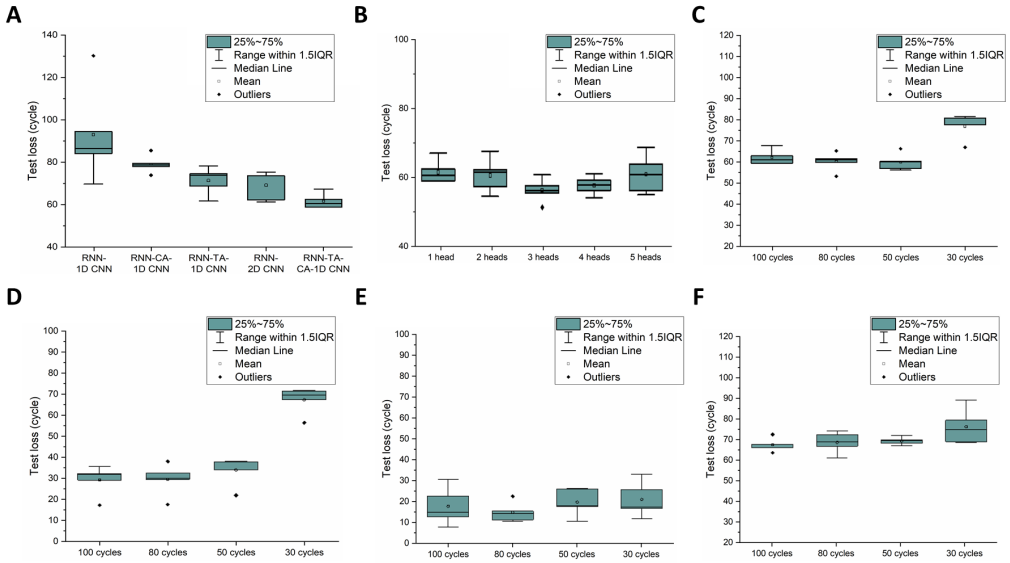


**Figure S7. Test losses with error bars for experiments with RNN + TA + CA + 1D CNN (SHA for CA).** (A) Comparison with RNN + 1D CNN, RNN + CA + 1D CNN, RNN + TA + 1D CNN, and RNN + 2D CNN, with best hyperparameter values when the combined dataset is used as an input with five random seeds (SHA is used for CA), (B) Impact of number of heads for CA, (C) Input reductions test results trained with all batches, (D) Input reductions test results trained with Batch 1, (E) Input reductions test results trained with Batch 2, (F) Input reductions test results trained with Batch 3.

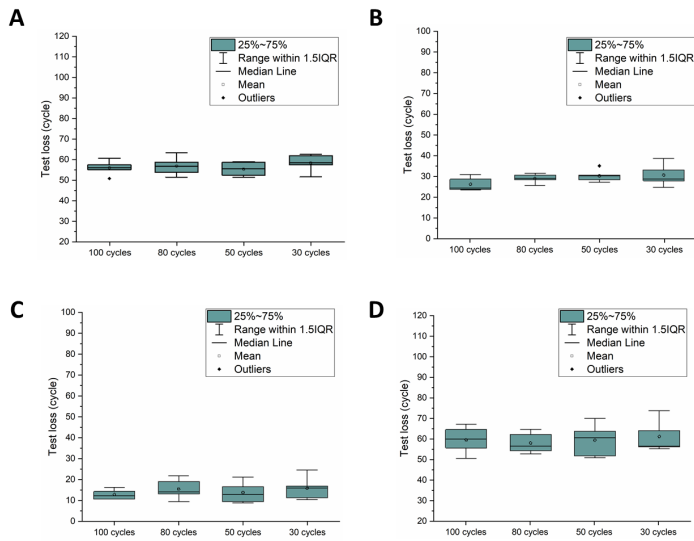


**Figure S8. Error bars of input reduction tests of RNN + TA + CA + 1D CNN (MHA for CA) trained with data from different batches.** (A) Input reductions test results trained with all batches, (B) Input reductions test results trained with Batch 1, (C) Input reductions test results trained with Batch 2, (D) Input reductions test results trained with Batch 3.

## Supplementary Tables

**Table S1.** Cell indexes, Charging policy, Calculated knee-onset. As listed in the reference<sup>1</sup>, ‘Charging policy’ refers to the C-rates between 0% and 80% of SOC and is formatted as “C1(Q1%)-C2”, where C1 and C2 represent the C-rates in the first and second phases, respectively, and Q1 represents the SOC where second phase starts.

index	policy	knee-onset
b1c0	3.6C(80%)-3.6C	1184.34
b1c1	3.6C(80%)-3.6C	1548.95
b1c2	3.6C(80%)-3.6C	1616.84
b1c3	4C(80%)-4C	842.03
b1c4	4C(80%)-4C	1006.22
b1c5	4.4C(80%)-4.4C	636.07
b1c6	4.8C(80%)-4.8C	435.91
b1c7	4.8C(80%)-4.8C	513.98
b1c9	5.4C(40%)-3.6C	653.80
b1c11	5.4C(50%)-3C	472.27
b1c14	5.4C(60%)-3C	469.17
b1c15	5.4C(60%)-3C	442.19
b1c16	5.4C(60%)-3.6C	508.01
b1c17	5.4C(60%)-3.6C	481.26
b1c18	5.4C(70%)-3C	534.55
b1c19	5.4C(70%)-3C	462.04
b1c20	5.4C(80%)-5.4C	156.01
b1c21	5.4C(80%)-5.4C	338.07
b1c23	6C(30%)-3.6C	584.05
b1c24	6C(40%)-3C	606.17
b1c25	6C(40%)-3C	477.18
b1c26	6C(40%)-3.6C	519.05
b1c27	6C(40%)-3.6C	517.98
b1c28	6C(50%)-3C	464.14
b1c29	6C(50%)-3C	512.14
b1c30	6C(50%)-3.6C	461.56
b1c31	6C(50%)-3.6C	535.01
b1c32	6C(60%)-3C	445.09
b1c33	6C(60%)-3C	454.85
b1c34	7C(30%)-3.6C	475.05
b1c35	7C(30%)-3.6C	428.85
b1c36	7C(40%)-3C	432.73
b1c37	7C(40%)-3C	396.73
b1c38	7C(40%)-3.6C	358.15
b1c39	7C(40%)-3.6C	368.04

b1c40	8C(15%)-3.6C	556.75
b1c41	8C(15%)-3.6C	608.28
b1c42	8C(25%)-3.6C	399.24
b1c43	8C(25%)-3.6C	395.03
b1c44	8C(35%)-3.6C	347.49
b1c45	8C(35%)-3.6C	349.14
b2c0	1C(4%)-6C	123.13
b2c1	2C(10%)-6C	45.09
b2c2	2C(2%)-5C	265.09
b2c3	2C(7%)-5.5C	124.18
b2c4	3.6C(22%)-5.5C	291.93
b2c5	3.6C(2%)-4.85C	299.01
b2c6	3.6C(30%)-6C	399.54
b2c10	3.6C(9%)-5C	354.97
b2c11	4C(13%)-5C	297.60
b2c12	4C(31%)-5	252.00
b2c13	4C(40%)-6C	316.00
b2c14	4C(4%)-4.85C	301.11
b2c17	4.4C(24%)-5C	308.17
b2c18	4.4C(47%)-5.5C	311.14
b2c19	4.4C(55%)-6C	344.84
b2c20	4.4C(8%)-4.85C	306.85
b2c21	4.65C(19%)-4.85C	298.32
b2c22	4.65C(44%)-5C	318.12
b2c23	4.65C(69%)-6C	336.69
b2c24	4.8C(80%)-4.8C	304.05
b2c25	4.8C(80%)-4.8C	286.11
b2c26	4.8C(80%)-4.8C	285.25
b2c27	4.9C(27%)-4.75C	279.13
b2c28	4.9C(61%)-4.5C	321.98
b2c29	4.9C(69%)-4.25C	311.29
b2c30	5.2C(10%)-4.75C	293.22
b2c31	5.2C(37%)-4.5C	304.48
b2c32	5.2C(50%)-4.25C	302.25
b2c33	5.2C(58%)-4C	329.1
b2c34	5.2C(66%)-3.5C	320.24
b2c35	5.2C(71%)-3C	299.09
b2c36	5.6C(25%)-4.5C	333.38
b2c37	5.6C(38%)-4.25C	307.58
b2c38	5.6C(47%)-4C	300.13
b2c39	5.6C(58%)-3.5C	289.04

b2c40	5.6C(5%)-4.75C	289.24
b2c41	5.6C(65%)-3C	270.46
b2c42	6C(20%)-4.5C	283.03
b2c43	6C(31%)-4.25C	272.15
b2c44	6C(40%)-4C	247.00
b2c45	6C(4%)-4.75C	307.27
b2c46	6C(52%)-3.5C	276.08
b2c47	6C(60%)-3C	456.22
b3c0	5C(67%)-4C	715.95
b3c1	5.3C(54%)-4C	740.77
b3c3	5.6C(36%)-4.3C	757.28
b3c4	5.6C(19%)-4.6C	676.78
b3c5	5.6C(36%)-4.3C	527.11
b3c6	3.7C(31%)-5.9C	433.40
b3c7	4.8C(80%)-4.8C	1283.97
b3c8	5C(67%)-4C	569.00
b3c9	5.3C(54%)-4C	672.26
b3c10	4.8C(80%)-4.8C	666.29
b3c11	5.6C(19%)-4.6C	495.04
b3c12	5.6C(36%)-4.3C	598.09
b3c13	5.6C(19%)-4.6C	496.91
b3c14	5.6C(36%)-4.3C	530.77
b3c15	5.9C(15%)-4.6C	529.99
b3c16	4.8C(80%)-4.8C	968.07
b3c17	5.3C(54%)-4C	837.13
b3c18	5.6C(19%)-4.6C	746.16
b3c19	5.6C(36%)-4.3C	762.07
b3c20	5C(67%)-4C	549.19
b3c21	3.7C(31%)-5.9C	537.88
b3c22	5.9C(60%)-3.1C	702.22
b3c24	5C(67%)-4C	533.15
b3c25	5.3C(54%)-4C	682.11
b3c26	5.6C(19%)-4.6C	647.27
b3c27	5.6C(36%)-4.3C	552.69
b3c28	3.7C(31%)-5.9C	339.59
b3c29	5.9C(15%)-4.6C	525.22
b3c30	5.3C(54%)-4C	638.72
b3c31	5.9C(60%)-3.1C	472.02
b3c33	5C(67%)-4C	931.00
b3c34	5.3C(54%)-4C	679.18
b3c35	5.6C(19%)-4.6C	665.08

b3c36	5.6C(36%)-4.3C	666.66
b3c38	5C(67%)-4C	1449.94
b3c39	5.3C(54%)-4C	841.11
b3c40	5.6C(19%)-4.6C	493.02
b3c41	5.6C(36%)-4.3C	502.75
b3c44	5.3C(54%)-4C	641.14
b3c45	4.8C(80%)-4.8C	947.22

**Table S2.** Tested hyperparameters of the neural networks. ( $n_{ep}$ : Number of epochs,  $f_i$ : Number of CNN initial filters,  $k_i$ : kernel size,  $n_p$ : Number of CNN pooling layers,  $n_{np}$ : Number of CNN non-pooling layers,  $h_i$ : RNN hidden size)

**Table S3.** Best choices of hyperparameters for the various models with the discharging dataset only.

	Learning rate	$f_i$	$k_i$	$n_p$	$n_{np}$	$h_i$
RNN + 1D CNN	1e-3	8	4	1	1	5
RNN + 2D CNN	1e-4	8	(3,4)	1	1	7
RNN + TA + 1D CNN	1e-2	7	3	2	1	5

**Table S4.** Best choices of hyperparameters for the various models with the charging dataset only.

	Learning rate	$f_i$	$k_i$	$n_p$	$n_{np}$	$h_l$
RNN + 1D CNN	1e-4	8	5	1	1	7
RNN + 2D CNN	1e-5	8	(3,5)	2	1	7
RNN + TA + 1D CNN	1e-2	5	3	1	2	5

**Table S5.** Best choices of hyperparameters for the various models with the combined dataset (including charging, discharging, and rest phases) (SHA is used for CA)

	Learning rate	$f_i$	$k_i$	$n_p$	$n_{np}$	$h_i$
RNN + 1D CNN	1e-2	8	4	2	1	5
RNN + 2D CNN	1e-3	8	(3,3)	2	1	7
RNN + TA + 1D CNN	1e-2	5	3	1	1	7
RNN + CA + 1D CNN	1e-2	7	3	2	1	3
RNN + TA + CA + 1D CNN	1e-2	5	3	2	1	7

**Table S6.** Best choices of hyperparameters for RNN + TA + CA + 1D CNN when multi-head attention is used for CA. (Input: 100 cycles of the combined dataset, including charging, discharging, and rest phases)

	Learning rate	$f_i$	$k_i$	$n_p$	$n_{np}$	$h_i$ per head
2 heads	1e-3	7	3	2	1	7
3 heads	1e-2	5	3	1	2	7
4 heads	1e-3	5	3	2	2	3
5 heads	1e-3	5	3	2	1	7

**Table S7.** Best choices of hyperparameters for RNN + TA + CA + 1D CNN for the input reduction test (All batches)

		Learning rate	$f_i$	$k_i$	$n_p$	$n_{np}$	$h_i$	per head
30 cycles	1 head	1e-2	3	3	1	1	3	
	3 heads	5e-4	5	3	2	1	3	
50 cycles	1 head	1e-2	3	3	1	1	3	
	3 heads	5e-3	3	3	1	1	3	
80 cycles	1 head	1e-4	3	3	1	1	3	
	3 heads	1e-4	5	3	2	1	3	

**Table S8.** Best choices of hyperparameters for RNN + TA + CA + 1D CNN for the input reduction test (Batch 1)

		Learning rate	$f_i$	$k_i$	$n_p$	$n_{np}$	$h_i$	per head
30 cycles	1 head	1e-2	3	3	1	1	3	
	3 heads	5e-3	7	3	2	1	3	
50 cycles	1 head	1e-2	3	3	1	1	3	
	3 heads	1e-2	7	3	2	1	3	
80 cycles	1 head	1e-2	5	3	1	2	3	
	3 heads	1e-4	5	3	2	1	5	

**Table S9.** Best choices of hyperparameters for RNN + TA + CA + 1D CNN for the input reduction test (Batch 2)

		Learning rate	$f_i$	$k_i$	$n_p$	$n_{np}$	$h_i$	per head
30 cycles	1 head	1e-2	5	3	1	2	3	
	3 heads	1e-2	5	3	2	1	7	
50 cycles	1 head	1e-2	7	3	1	2	7	
	3 heads	1e-2	7	3	1	1	3	
80 cycles	1 head	5e-3	5	3	1	1	3	
	3 heads	1e-4	5	3	1	2	3	

**Table S10.** Best choices of hyperparameters for RNN + TA + CA + 1D CNN for the input reduction test (Batch 3)

		Learning rate	$f_i$	$k_i$	$n_p$	$n_{np}$	$h_i$	per head
30 cycles	1 head	1e-2	5	3	1	1	3	
	3 heads	1e-4	3	3	1	1	5	
50 cycles	1 head	1e-4	5	3	2	1	7	
	3 heads	1e-4	3	3	1	2	3	
80 cycles	1 head	1e-4	3	3	2	1	5	
	3 heads	1e-2	5	3	1	2	5	

## Supplementary Notes

### Note S1. Dataset description

In this part, we describe the Severson dataset<sup>1</sup> and some steps we performed to characterize and preprocess it. Since detailed explanations of the whole dataset were given in the reference<sup>2</sup>, we focus on the differences among the three different batches operating protocols and their effect on the knee-onset. Among the several available public datasets for LIB degradation<sup>3,4</sup>, the Severson dataset is chosen as it is a relatively large dataset involving 124 normal cells. This dataset was collected under a well-controlled setup, keeping the environmental variables (e.g., ambient temperature) constant. Therefore, it has become a popular benchmark dataset to test data-driven modeling approaches in the literature<sup>5,6</sup>.

Let us briefly discuss the main features of the dataset. Each cell was subjected to repeated tests of charging-discharging cycles until its EOL. During the charging phase, one or two-step constant current (CC) policies were applied up to 80% SOC. Then, a certain amount of rest time was placed (details will be discussed shortly). After the rest, a constant voltage (CV) charging policy was applied to reach 100% SOC. The discharging phase employed the same 4C CC policy for all the cells. Finally, the discharging was followed by another rest time to complete the cycle. The dataset encompasses three batches of data, which feature different rest time characteristics. In Batch 1, different rest times were applied after 80% SOC charging (1 min) and after discharging (1 sec), while the same rest time was used for both rests in Batch 2 (5 min) and Batch 3 (5 sec). In Batch 3, two additional rests of 5 sec were applied after the IR test and before the discharging.

[Figure S1A](#) shows each batch's average C-rate until 80% SOC (end of CC policy) and IR values (averaged only for the last 100 cycles of each cell). The average C-rate until 80% SOC of batch  $b_l$ ,  $cr_{b_l}$ , can be calculated using the following Eq. (3).

$$cr_{b_l} = \frac{\sum_{m=1}^{n_{b_l}} \left( \frac{cr_{1st}^{ce_m} Q_{tr}^{ce_m}}{80} + \frac{cr_{2nd}^{ce_m} (80 - Q_{tr}^{ce_m})}{80} \right)}{n_{b_l}} \quad (1)$$

where  $n_{b_l}$  is the number of cells belonging to batch  $b_l$ ,  $Q_{tr}^{ce_m}$ (%) is the point of transition from the 1st to 2nd charging step for cell  $ce_m$ , and  $cr_{1st}^{ce_m}$  and  $cr_{2nd}^{ce_m}$  are the C-rates of the 1st charging step (0- $Q_{tr}^{ce_m}$ % SOC) and the 2nd charging step ( $Q_{tr}^{ce_m}$ -80% SOC) for cell  $ce_m$  of batch  $b_l$ , respectively. Looking at  $cr_{b_l}$  of each batch, although different charging policies were applied (72 policies in total), the average charging rate varies by very little across the batches. We can also see that Batch 2 has the largest IR value, followed by Batch 1 and Batch 3, exactly matching the order of the rest times. In Keil et al.<sup>7</sup>, it was shown that an increase in rest time led to a considerable increase in IR, and such an increase is accelerated when the SOC is large. As mentioned above, in the Severson dataset, the rest occurs once at 80% SOC, leading to a significant increase in IR (especially for Batch 2).

[Figure S1B](#) summarizes the average and standard deviation of knee-onset for each batch. In Celik et al.<sup>8</sup>, it was analyzed that the Spearman coefficient between the IR and the cycle life in the Severson dataset was -0.6517, implying a strong correlation between them, which can be confirmed by inspecting [Figure S1A-B](#). Looking at the standard deviations of the knee-onset, larger variations can be observed for Batch 1 and Batch 3 compared to Batch 2. This is mainly due to the relatively short lifespans of the cells in Batch 2.

Based on the above, it can be argued that it is important for a knee-onset regression model to achieve small errors for Batches 1 and 3, which exhibit large variations in the lifespan. Rest time, a design variable for cycling tests (thus readily available), has the potential to be used as an indicator of IR, which is expensive to measure. These ideas will be tested using the data-driven models described subsequently.

In our test, the number of initial cycles in the input data to predict knee onset will vary.

Specifically,  $n_{cy}$  takes different values (30, 50, 80, and 100), with 100 being the base case value. Within each cycle, samples are taken with a 0.5 min interval up to 60 min (i.e.,  $n_{ts} = 120$ ), and zero-padding is used when needed to accommodate variable cycle lengths. When using the charging-only dataset with only the measurements taken during charging operations, we use  $V, I, T$  and  $Q_c$  as the inputs with  $n_{ts} = 40$ . On the other hand, when using the discharging-only dataset,  $dQ/dV, Q_d, T$  are used as the inputs. The input dataset is rearranged with respect to voltage (as a surrogate of time) since only constant-current policy is used in the discharging phase, and  $n_{ts}$  is selected as 1000 points. The reasons for these choices were explained in our previous work<sup>2</sup>.

## Supplementary References

1. Severson, K.A., Attia, P.M., Jin, N., Perkins, N., Jiang, B., Yang, Z., Chen, M.H., Aykol, M., Herring, P.K., and Fragedakis, D. (2019). Data-driven prediction of battery cycle life before capacity degradation. *Nature Energy* 4, 383-391.
2. Lee, J., and Lee, J.H. (2024). Simultaneous extraction of intra-and inter-cycle features for predicting lithium-ion battery's knees using convolutional and recurrent neural networks. *Applied Energy* 356, 122399.
3. Saha, B., and Goebel, K. (2007). Battery data set. NASA AMES prognostics data repository.
4. He, W., Williard, N., Osterman, M., and Pecht, M. (2011). Prognostics of lithium-ion batteries based on Dempster–Shafer theory and the Bayesian Monte Carlo method. *Journal of Power Sources* 196, 10314-10321.
5. Chen, Z., Shi, N., Ji, Y., Niu, M., and Wang, Y. (2021). Lithium-ion batteries remaining useful life prediction based on BLS-RVM. *Energy* 234, 121269.
6. Li, W., Sengupta, N., Dechent, P., Howey, D., Annaswamy, A., and Sauer, D.U. (2021). One-shot battery degradation trajectory prediction with deep learning. *Journal of Power Sources* 506, 230024.
7. Keil, P., and Jossen, A. (2015). Aging of lithium-ion batteries in electric vehicles: Impact of regenerative braking. *World Electric Vehicle Journal* 7, 41-51.
8. Celik, B., Sandt, R., dos Santos, L.C.P., and Spatschek, R. (2022). Prediction of battery cycle life using early-cycle data, machine learning and data management. *Batteries* 8, 266.